

# Microlensing of lensed supernovae Zwicky & iPTF16geu: constraints on the lens galaxy mass slope and dark compact object fraction

NIKKI ARENDSE<sup>1</sup>, EDVARD MÖRTSELL<sup>1</sup>, LUKE WEISENBACH<sup>2</sup>, ERIN HAYES<sup>3</sup>, STEPHEN THORP<sup>1,3</sup>, SUHAIL DHAWAN<sup>3,4</sup>, ARIEL GOOBAR<sup>1</sup>, SACHA GUERRINI<sup>5</sup>, JACOB OSMAN HJORTLUND<sup>1</sup>, JOEL JOHANSSON<sup>1</sup>, CAMERON LEMON<sup>1</sup>, AND ABDULLAH AL ZAIF<sup>3</sup>

<sup>1</sup> Oskar Klein Centre, Department of Physics, Stockholm University, SE-106 91 Stockholm, Sweden

<sup>2</sup> Institute of Cosmology and Gravitation, University of Portsmouth, Burnaby Road, Portsmouth, PO1 3FX, UK

<sup>3</sup> Institute of Astronomy and Kavli Institute for Cosmology, University of Cambridge, Madingley Road, Cambridge CB3 0HA, UK

<sup>4</sup> School of Physics and Astronomy, University of Birmingham, Birmingham, UK and

<sup>5</sup> Université Paris Cité, Université Paris-Saclay, CEA, CNRS, AIM, 91191, Gif-sur-Yvette, France

*Version November 11, 2025*

## ABSTRACT

To date, only two strongly lensed type Ia supernovae (SNIa) have been discovered with an isolated galaxy acting as the lens: iPTF16geu and SN Zwicky. The observed image fluxes for both lens systems were inconsistent with predictions from a smooth macro lens model. A potential explanation for the anomalous flux ratios is microlensing: additional (de)magnification caused by stars and other compact objects in the lens galaxy. In this work, we combine observations of iPTF16geu and SN Zwicky with simulated microlensing magnification maps, leveraging their standardizable candle properties to constrain the lens galaxy mass slope,  $\eta$ , and the fraction of dark compact objects,  $f_{dc}$ . The resulting mass slopes are  $\eta = 1.70 \pm 0.07$  for iPTF16geu and  $\eta = 1.81 \pm 0.10$  for SN Zwicky. Our results indicate no evidence for a population of dark compact objects, placing upper limits at the 95% confidence level of  $f_{dc} < 0.25$  for iPTF16geu and  $f_{dc} < 0.47$  for SN Zwicky (for compact objects with masses above  $0.02M_{\odot}$ ). Assuming a constant fraction of dark compact objects for both lensed SNe, we obtain  $f_{dc} < 0.19$ . These results highlight the potential of strongly lensed SNIa to probe the innermost parts of lens galaxies and learn about compact matter.

## 1. INTRODUCTION

Strong gravitational lensing occurs when light from a distant light source is deflected by the gravitational potential of a massive galaxy or galaxy cluster along the line of sight, resulting in multiple images of the event. When the light source is a transient event, such as a supernova (SN), we can measure the time delays between the appearance of the multiple images. Combined with a model for the gravitational potential of the lens galaxy and line-of-sight structures, this constrains the present-day expansion rate of the Universe, the Hubble constant  $H_0$  (Refsdal 1964; Treu & Marshall 2016; Suyu et al. 2024; Birrer et al. 2024). Additionally, lensed SNe enable detailed studies of lensing galaxies and high-redshift SNe (Cano et al. 2018; Johansson et al. 2021; Dhawan et al. 2024).

While strongly lensed SNe are very useful, they are also extremely rare and challenging to discover. To date, only eight multiply-imaged lensed SNe have been found. Six of them have been discovered behind galaxy clusters: ‘SN Refsdal’ (Kelly et al. 2015), ‘SN Requiem’ (Rodney et al. 2021), ‘AT2022riv’ (Kelly et al. 2022), ‘C22’ (Chen et al. 2022), ‘SN H0pe’ (Frye et al. 2024), and ‘SN Encore’ (Pierel et al. 2024). Additionally, two lensed SNe were lensed by isolated elliptical galaxies: ‘iPTF16geu’ (Goobar et al. 2017) and ‘SN Zwicky’ (Goobar et al. 2023), shown in Fig. 1. Both of these galaxy-scale lensed

SNe were type Ia SNe (SNIa) that were recognised as being gravitationally lensed from their brightness relative to their redshifts. This could be inferred thanks to their standardizable-candle nature, and because they were bright enough to obtain a spectroscopic redshift. iPTF16geu was found with the intermediate Palomar Transient Factory (iPTF), a time-domain survey that ran from 2013 to 2017 (Kulkarni 2013). From 2018 onwards, a new camera with a larger field of view was installed on the telescope and the survey continued as the Zwicky Transient Facility (ZTF; Bellm et al. 2019; Graham et al. 2019). After four years of ZTF observations, SN Zwicky was discovered. Simulation studies show that a handful more, unidentified, lensed SNe are expected to be present in the ZTF data below the spectroscopic follow-up limit (Sagués Carracedo et al. 2024). Archival studies have been conducted to search for these overlooked lensed SNe (Magee et al. 2023; Townsend et al. 2025), and in Townsend et al. (2025), two potential lensed SNe are identified. The number of lensed SN detections is expected to increase orders of magnitudes with the upcoming Vera Rubin Observatory (Wojtak et al. 2019; Goldstein et al. 2019; Oguri & Marshall 2010; Sainz de Murieta et al. 2023; Arendse et al. 2024).

iPTF16geu and SN Zwicky share several characteristics: they are both highly magnified ( $67.8 \pm 2.9$  and  $23.7 \pm 3.2$  times, respectively) and have short time delays of the order of a day (More et al. 2017; Dhawan et al. 2020; Goobar et al. 2023). Additionally, they are unusu-

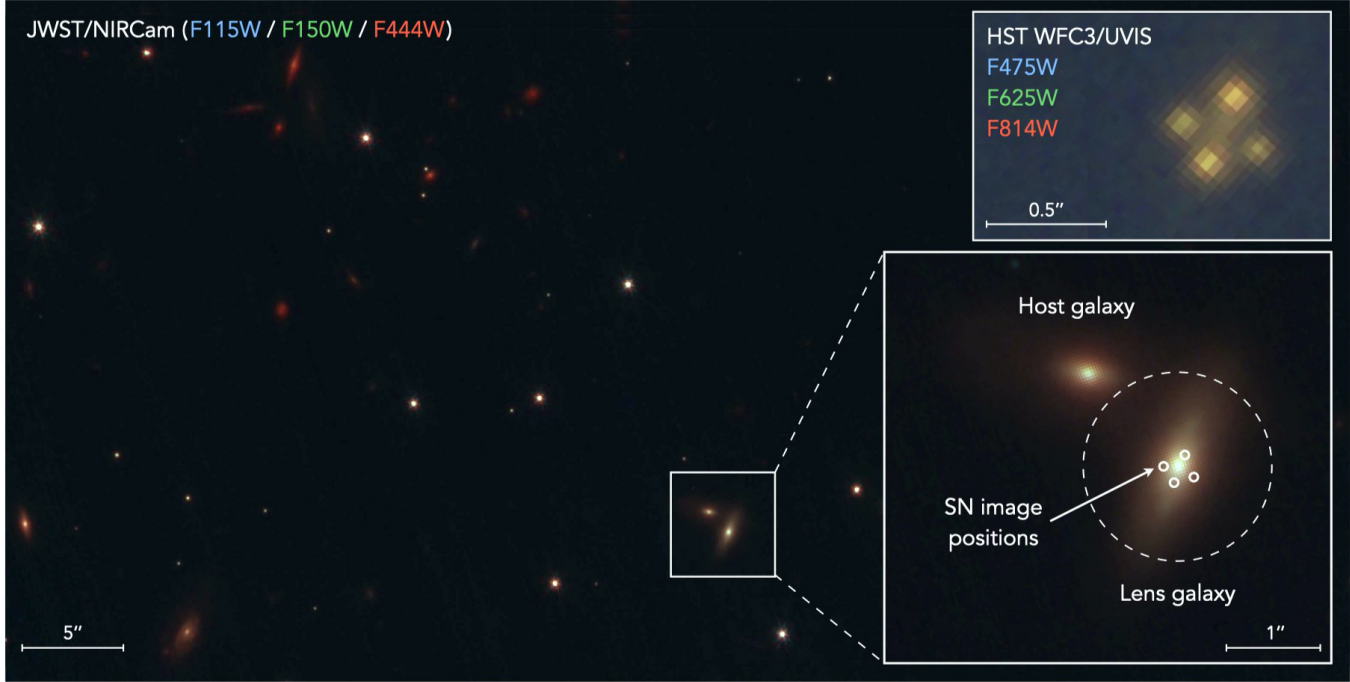


FIG. 1.—: *JWST* image of the field of SN Zwicky post-explosion, showing its lens and host galaxies. The upper right inset shows SN Zwicky when it was active in earlier *HST* observations. The lower right inset provides a zoomed-in view of the *JWST* field, showing the lens galaxy and the host galaxy, which is not strongly lensed. The SN image positions are derived from the *HST* observations and projected onto the observations as white circles. The dashed circle with a  $1''$  radius indicates the aperture within which the stellar mass measurement of the lens galaxy has been conducted.

ally compact lens systems: iPTF16geu has an Einstein radius of  $0.29''$  and SN Zwicky of only  $0.17''$ . Compared to the population of known lensed galaxies and lensed quasars, both are outliers with small Einstein radii and faint lens galaxies, and they were only identified because they magnified SNIa standard candles (see [Lemon et al. 2024](#), and Fig. 4 in [Goobar et al. 2023](#)). Another interesting shared property is that the flux ratios of their lensed images, after corrections for differential dust extinction in the lensing galaxy, are inconsistent with predicted flux ratios from a smooth macro lens model ([More et al. 2017](#); [Mörtzell et al. 2020](#); [Goobar et al. 2023](#); [Pierel et al. 2023](#)). A potential explanation for the observed fluxes is additional (de)magnification from stars, stellar remnants and other compact objects in the lens galaxy; known as *microlensing* ([Chang & Refsdal 1979](#)). Several papers have analysed SN Zwicky and found evidence that microlensing is needed to explain the observed flux ratios ([Goobar et al. 2023](#); [Pierel et al. 2023](#); [Larison et al. 2024](#)). Lensing at such small angular scales ( $\sim 10^{-6}''$ ) results in unresolvable micro-images that sum to a total magnification which differs from the macro magnification of the lens galaxy ([Young 1981](#); [Paczynski 1986](#); [Vernardos et al. 2024](#)). This process perturbs the magnification of each image independently, resulting in flux ratios that are discrepant from the macro model predictions. Microlensing is often talked about in terms of complicating the use of lensed SNIa for time-delay cosmography ([Dobler & Keeton 2006](#); [Yahalomi et al. 2017](#); [Foxley-Marrable et al. 2018](#); [Weisenbach et al. 2021, 2024](#)). However, the combination of microlensing and lensed SNe Ia offers a unique opportunity: since SNe Ia are standardiz-

able candles with predictable brightness for each lensed image, we are able to precisely detect the magnification contribution from microlensing.

Microlensing allows us to probe the abundance of compact objects at the image positions, even if they are dark or too faint to observe. This makes microlensing a unique probe to distinguish between the smooth and compact matter components of the lens galaxy. By comparing the fraction of compact objects inferred from microlensing to the stellar mass fraction determined from photometry, we can determine if there are signs of an additional population of dark compact objects, such as primordial black holes (PBHs). PBHs are hypothetical black holes that formed in the early Universe through direct gravitational collapse (e.g. [Khlopov 2010](#); [Carr et al. 2016](#); [Escrivà et al. 2024](#)). Since they are not formed through stellar collapse, their masses are not limited to the narrow mass range of stellar black holes. PBHs are candidates for part of the dark matter in the Universe, as well as potential seeds for supermassive black holes. In particular, gravitational wave observations from the Laser Interferometer Gravitational-Wave Observatory (LIGO) suggest that PBHs of intermediate mass ( $10M_{\odot} < M < 200M_{\odot}$ ) may constitute a substantial part of the dark matter in the Universe ([Clesse & García-Bellido 2015](#); [Kashlinsky 2016](#); [Hawkins 2020](#)), which we could detect through microlensing observations.

Microlensing flux ratio studies have been conducted extensively for strongly lensed quasars (e.g. [Chang & Refsdal 1979](#); [Wambsganss 2006](#); [Schmidt & Wambsganss 2010](#); [Vernardos & Tsagkatakis 2019](#); [Vernardos](#)

## Photometric observations and filters used

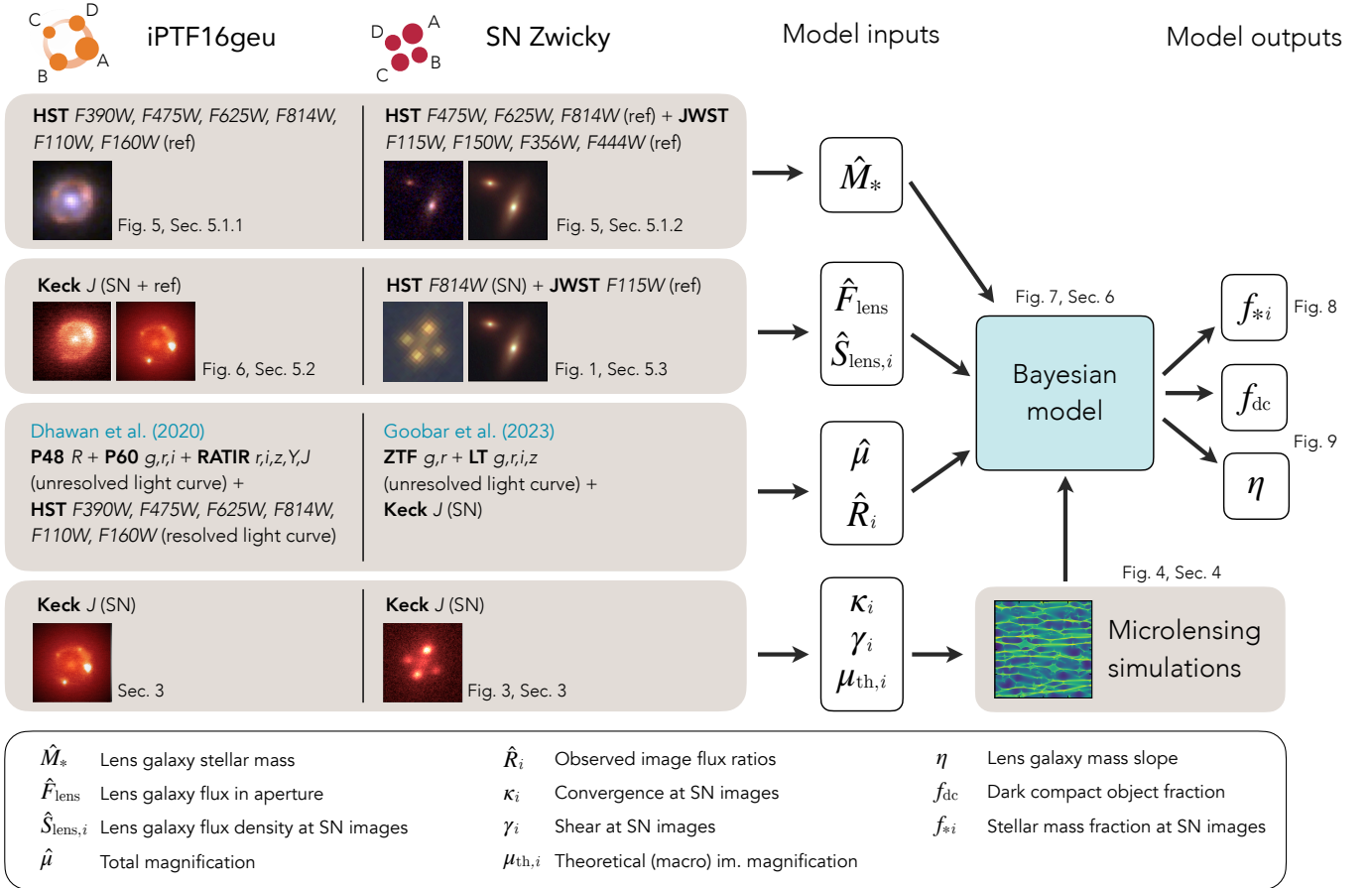


FIG. 2.—: Flowchart of the observations and inferred quantities of this work. The left shaded panels show the specific observations and filters that go into modelling the derived quantities in the middle column, which in turn serve as input for the microlensing simulations and our Bayesian model. The final outputs, shown on the right, are the lens galaxy mass slope,  $\eta$ , fraction of dark compact objects,  $f_{\text{dc}}$ , and the stellar mass fraction at the SN image positions,  $f_{*,i}$ .

et al. 2024), of which several studies have constrained the abundance of compact objects through microlensing (e.g. Pooley et al. 2009, 2012; Schechter & Wambsganss 2004; Schechter et al. 2014; Mediavilla et al. 2009, 2017; Esteban-Gutiérrez et al. 2020; Mediavilla & Jiménez-Vicente 2025). Most of these studies conclude that the compact objects causing microlensing can be explained sufficiently by the normal stellar population, and the fraction of dark compact objects is constrained to be below 10% for masses above  $0.002M_{\odot}$  (Esteban-Gutiérrez et al. 2023; Mediavilla & Jiménez-Vicente 2025). For galaxy-scale lensed SNe, the field of microlensing studies has only recently opened up, with iPTF16geu the first object that allowed such investigation. In Mörtsell et al. (2020), microlensing was included in the analysis of the image magnifications to obtain the lens galaxy mass slope,  $\eta \sim 1.8$ . Diego et al. (2022) studied the observed flux ratios and light curves of iPTF16geu and concluded that microlensing effects from stars suffice to explain the data. With the discovery of SN Zwicky, a second galaxy-scale lensed SN has become available to study microlensing. In this work, we perform a micro and macro lensing analysis of photometric observations of SN Zwicky and iPTF16geu, and develop a Bayesian

model to constrain the lens galaxy mass slopes and compact objects fractions. By combining these with stellar mass fractions measured from photometry data, we estimate how much of the mass can be in the form of dark compact objects.

We describe the observations used in this work in section 2, the macrolens model in section 3, and our microlensing simulations in section 4. In section 5, we describe the lens galaxy stellar mass and light analyses, and in section 6 we outline our Bayesian model. Section 7 shows our results, and section 8 gives our discussion and conclusions. A flowchart of the data we use, inferred quantities, and the input and output of the Bayesian model is presented in Fig. 2.

## 2. OBSERVATIONS

Here, we summarise the observations of iPTF16geu and SN Zwicky used in our analysis. More elaborate descriptions can be found in Goobar et al. (2017); Dhawan et al. (2020); Goobar et al. (2023); Pierel et al. (2023).

### 2.1. iPTF16geu

SN iPTF16geu was discovered in 2016 with iPTF. Spectroscopic identification was carried out with Spec-

tral Energy Distribution Machine (SEDM; [Blagorodnova et al. 2018; Rigault et al. 2019](#)) at the Palomar 60-inch telescope on 2 October 2016, and iPTF16geu was found to be consistent with a SNIa at  $z = 0.4$ . For the purposes of this work, we focus on the high-resolution imaging data from the Keck II telescope on Mauna Kea and the *Hubble Space Telescope* (*HST*). The observations from the Keck telescope used in this work were conducted with the Near-IR Camera 2 (NIRC2; [Fremling et al. 2022](#)) in the  $J$ -band, using laser guided adaptive optics (LGS-AO). Details of the reduction can be found in [Goobar et al. \(2017\); Dhawan et al. \(2020\)](#). The *HST* data were taken with the Wide Field Camera 3, using the UV (WFC3/UVIS) and near-IR (WFC3/IR) channels. There were two epochs of observations in the  $F390W$ ,  $F475W$  filters and eight epochs in each of the  $F625W$ ,  $F814W$ ,  $F110W$ , and  $F160W$  filters. After the SN faded, we obtained reference observations in each of the filters on 2018 November 10. The reference images both for the ground-based and *HST* data are a crucial benefit of lensed SNe, since we can model the lensed host galaxy without the presence of the point sources.

## 2.2. SN Zwicky

On August 2022, SN Zwicky was discovered with ZTF. The object was bright enough for an automatic classification with SEDM, where a spectrum taken on the 21st of August showed it to be a SNIa at a redshift of  $z = 0.35$ , confirming a brightness several magnitudes brighter than a typical SNIa at that redshift. The multiple images of SN Zwicky were first resolved on 2022 September 15 with the Keck telescope in the  $J$ -band, using adaptive optics with the NIRC2 camera ([Fremling et al. 2022](#)). On September 21, the LensWatch collaboration<sup>1</sup> observed SN Zwicky using *HST* with the optical filters  $F475W$ ,  $F625W$  and  $F814W$  (WFC3/UVIS Camera) and the NIR  $F160W$  filter (WFC3/IR) ([Pierel et al. 2022, 2023](#)). To allow for further studies of the lens and host galaxies, reference images after SN Zwicky faded were obtained with *HST* in the same filters ([Larison et al. 2024](#)) and also with the *James Webb Space Telescope* (*JWST*)<sup>2</sup> in the filters  $F115W$ ,  $F150W$ ,  $F356W$ , and  $F444W$ , as shown in a composite image in Fig. 1.

## 3. MACRO LENS MODELLING

We describe the definitions of our mass and light models in section 3.1, our fitting methodology in section 3.3, and explain how we constrain the galaxy mass slope from standard candle magnifications in section 3.4.

### 3.1. Mass and light model definitions

We model the mass distribution in the lens galaxies of SN Zwicky and iPTF16geu as a power-law elliptical mass distribution (PEMD):

$$\kappa(x, y) = \frac{3 - \eta}{2} \left( \frac{\theta_E}{\sqrt{qx^2 + y^2/q}} \right)^{\eta-1}, \quad (1)$$

where  $\kappa$  is the projected surface mass density (convergence),  $q$  denotes the projected axis ratio of the lens,  $\theta_E$

is the Einstein radius, and  $\eta$  corresponds to the logarithmic lens mass slope. The coordinates  $(x, y)$  are centred on the lens galaxy mass centre and are rotated by the lens orientation angle  $\phi$  so that the  $x$ -axis aligns with the major axis of the lens.

We model the light of the lens and host galaxies in the form of elliptical Sérsic profiles:

$$I(R) = I_e \exp \left\{ -b_n \left[ \left( \frac{R}{R_e} \right)^{1/n} - 1 \right] \right\}, \quad (2)$$

where  $I_e$  is the intensity at the half-light radius  $R_e$ ,  $b_n = 1.9992n - 0.3271$  ([Birrer & Amara 2018](#)) and

$$R \equiv \sqrt{x^2 + y^2/q_s^2}, \quad (3)$$

with  $q_s$  the axis ratio of the Sérsic profile and  $(x, y)$  the coordinates that are centred on the lens galaxy light centre and rotated by the orientation angle  $\phi_s$ . The multiple lensed images of the SNe are modelled as point sources, where the Point Spread Function (PSF) was obtained by fitting a Moffat profile to stars in the field, where possible (e.g. *HST* and *JWST*). In observations with no suitable stars (e.g. Keck), the SN images themselves were used for the PSF modelling.

### 3.2. Testing angular complexity in the mass model

To investigate whether deviations from a smooth elliptical mass distribution can account for the observed flux anomalies in the SN images, we tested the inclusion of multipole perturbations in the lens model. Recent work by [Cohen et al. \(2024\)](#) has shown that higher-order angular structure in the lens galaxy can also reproduce flux-ratio anomalies, potentially providing an alternative explanation to microlensing. Specifically, we considered both circular and elliptical fourth-order multipole perturbations to the convergence, following the formalism of [Xu et al. \(2013\)](#) as implemented in the open-source lens modelling software *Lenstronomy*<sup>3</sup> ([Birrer & Amara 2018; Birrer et al. 2021](#)). The fourth-order multipole was added as an additional mass component with two free parameters: the amplitude  $a_4$  and the phase  $\phi_4$ . These multipole terms allow for departures from purely elliptical isodensity contours, introducing boxy or disk-like shapes. We applied this extended mass model to Keck  $J$ -band observations of both SN Zwicky and iPTF16geu, fixing the mass slope  $\eta$  to our best-fit values. The flux ratios of the SN images were included in the likelihood function to assess whether the lens model could reproduce them.

We briefly describe our main findings here. Our results for iPTF16geu yield a poor fit, with a high reduced  $\chi^2$  value. This demonstrates that even with the included angular complexity in the mass distribution, the lens model fails to reproduce the observed flux ratios. For SN Zwicky, the multipole model matches the observed flux ratios more closely, but the resulting mass distribution is highly irregular and unphysical, with best-fit multipole amplitudes ( $a_4 = -0.192^{+0.007}_{-0.005}$  for circular multipoles

<sup>1</sup> <https://www.lenswatch.org/home>

<sup>2</sup> Program ID: GO-2905

<sup>3</sup> <https://lenstronomy.readthedocs.io/en/latest/>

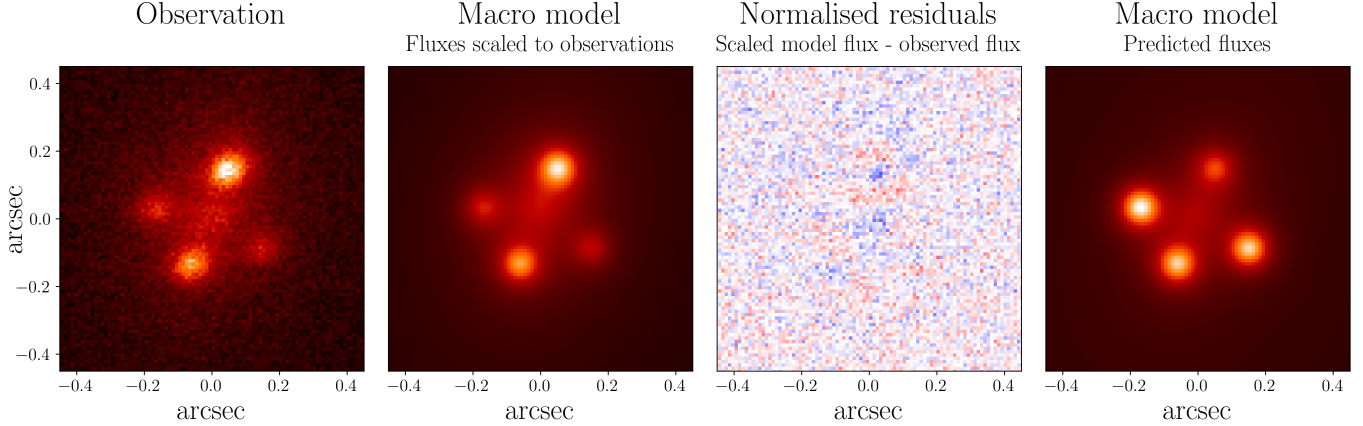


FIG. 3.—: The macrolens model fit and residuals to Keck  $J$ -band observations of SN Zwicky, using a PEMD model with a mass slope of  $\eta = 1.8$ . From left to right, the panels show: 1.) Keck  $J$ -band observations of SN Zwicky. 2.) The best-fit macro lens model with the SN image fluxes scaled to match the observed fluxes. Only the SN image positions are used to fit the macro lens model, because the fluxes are affected by microlensing. 3.) Normalised residuals between panels 2 and 1, demonstrating an excellent fit when SN fluxes are scaled. 4.) The predicted fluxes from the best-fit macro model, which deviate from the observed fluxes. This discrepancy highlights the effects of microlensing, which is not captured by the macro model.

and  $a_4 = -0.103^{+0.006}_{-0.005}$  for elliptical multipoles) inconsistent with realistic galaxy profiles (which are often of the order  $10^{-2}$ , see e.g. Hao et al. 2006). These unphysical multipole amplitudes are likely a consequence of the absence of a lensed host galaxy in the SN Zwicky observations, which would otherwise have constrained the model to more realistic values, as is the case for iPTF16geu. We conclude that angular complexity does not provide a plausible physical explanation for the observed flux ratios in either lensed SN system. These results strengthen the case that microlensing is required to explain the observed flux anomalies.

When the flux ratio constraints are excluded, adding multipole perturbations to the lens model decreases the reduced  $\chi^2$  by only 0.008 for iPTF16geu and provides no improvement for SN Zwicky. In our subsequent analysis, we do not include angular complexity and proceed with the mass model described in Section 3.1.

### 3.3. Fitting methodology

Using Lenstronomy, we simultaneously reconstruct the lens mass model, SN image positions, and the light distributions of the lens and host galaxy. For both iPTF16geu and SN Zwicky, we perform lens modelling for several observations from different telescopes and in different filters, each with characteristics that require slightly different approaches to the modelling. In this section, we outline our overarching modelling approach which applies to most observations, and we highlight deviations from this for specific cases in their respective sections.

Most of our lens models have the following 25 nonlinear parameters:

- **Lens galaxy mass model (PEMD):** Einstein radius ( $\theta_E$ ), axis ratio ( $q_{\text{lens}}$ ), orientation angle ( $\phi_{\text{lens}}$ ), lens galaxy mass centre ( $x_{\text{lens}}, y_{\text{lens}}$ ). Note that for most runs, the power-law slope of the mass profile,  $\eta$ , is not a free parameter, but fixed to specific values (as explained further in section 3.4).

- **Lens galaxy light model (Sérsic):** Sérsic radius ( $R_{s,\text{lens}}$ ), Sérsic index ( $n_{s,\text{lens}}$ ), axis ratio ( $q_{s,\text{lens}}$ ), orientation angle ( $\phi_{s,\text{lens}}$ ), lens galaxy light centre ( $x_{s,\text{lens}}, y_{s,\text{lens}}$ ).

- **Host galaxy light model:** Sérsic radius ( $R_{s,\text{host}}$ ), Sérsic index ( $n_{s,\text{host}}$ ), axis ratio ( $q_{s,\text{host}}$ ), orientation angle ( $\phi_{s,\text{host}}$ ), lens galaxy light centre ( $x_{s,\text{host}}, y_{s,\text{host}}$ ).

- **SN images:** positions of four point sources ( $x_A, y_A, x_B, y_B, x_C, y_C, x_D, y_D$ ).

Note that since the host galaxy of SN Zwicky is located at a large offset ( $\sim 1.4''$ ) from the lens galaxy centre, and it is not strongly lensed, the host galaxy light model is not always included in the lens modelling.

We iterate three times over fitting preliminary models with particle swarm optimization (PSO). For each of the three runs of PSO, we use 100, 100, and 10 particles and 100, 100, and 10 iterations, respectively. For the first run, we initialise the particles according to wide Gaussian priors around the expected parameter values. For the second and third runs, we reduce the standard deviations of the particle initial positions to 10% and 1% of their original values, respectively, around the best fit parameter values from the previous PSO iteration. We also iterate over the PSF model, using a built-in feature in Lenstronomy that minimises the residuals between the observed and reconstructed image around the SN positions (Shajib et al. 2019). Once a suitable PSF is obtained, we run a Markov chain Monte Carlo (MCMC) sampler to obtain parameter estimates with uncertainties. In particular, we use an affine invariant MCMC ensemble sampler from python package emcee (Foreman-Mackey et al. 2013; Goodman & Weare 2010). We typically use 200 walkers with 500 burn-in steps that we discard and 1500 steps from which we obtain the final posterior on the model parameters. Because we have already used PSO to bring the fitter close to the posterior maximum, we initialize the walkers with a standard deviation of 2% of that specified in the Gaussian priors.

TABLE 1: The macro lens modelling predictions for the convergence ( $\kappa$ ), shear ( $\gamma$ ), and magnifications ( $\mu$ ) at the image positions of iPTF16geu and SN Zwicky, for different lens galaxy mass slopes  $\eta$ . ‘A’, ‘B’, ‘C’, and ‘D’ correspond to the lensed SN images, and  $\Sigma = A + B + C + D$ , which is used to denote the total magnification. The predicted macro magnifications are discrepant with the observed magnifications, pointing to the presence of additional microlensing magnification. The  $\kappa$  and  $\gamma$  values serve as input for the microlensing simulations, together with the compact object fraction.

iPTF16geu													
$\eta$ (slope)	$\kappa$ (convergence)				$\gamma$ (shear)				$\mu$ (macro magnification)				
	A	B	C	D	A	B	C	D	A	B	C	D	$\Sigma$
2.10	0.53	0.36	0.55	0.39	0.63	0.46	0.65	0.49	5.79	5.35	4.78	7.91	23.8
2.05	0.55	0.39	0.57	0.42	0.60	0.44	0.62	0.47	6.81	6.11	5.63	9.04	27.6
2.00	0.57	0.43	0.58	0.45	0.57	0.43	0.58	0.45	7.69	6.79	6.39	10.0	30.9
1.95	0.58	0.46	0.59	0.48	0.53	0.41	0.54	0.43	8.85	7.67	7.34	11.3	35.2
1.90	0.60	0.49	0.62	0.51	0.50	0.39	0.51	0.41	10.3	8.74	8.52	12.9	40.5
1.85	0.62	0.52	0.64	0.54	0.47	0.37	0.48	0.38	11.1	9.44	9.33	14.0	43.9
1.80	0.65	0.54	0.66	0.56	0.45	0.34	0.46	0.36	13.1	10.9	11.0	16.2	51.2
1.75	0.66	0.57	0.67	0.59	0.42	0.33	0.42	0.34	15.4	12.7	13.0	18.9	60.0
1.70	0.69	0.60	0.70	0.62	0.39	0.31	0.39	0.32	18.2	14.9	15.4	22.2	70.7
1.65	0.71	0.63	0.72	0.65	0.36	0.29	0.36	0.29	23.4	18.7	19.7	27.9	89.7
1.60	0.73	0.66	0.74	0.68	0.33	0.26	0.33	0.27	27.4	21.8	23.2	32.6	105
1.55	0.75	0.69	0.76	0.70	0.30	0.24	0.31	0.25	33.6	26.5	28.5	39.7	128
1.50	0.77	0.72	0.78	0.73	0.27	0.22	0.28	0.23	42.1	33.0	35.7	49.3	160
1.45	0.80	0.75	0.80	0.76	0.25	0.20	0.25	0.20	53.4	41.4	45.4	62.2	202
1.40	0.82	0.77	0.82	0.79	0.22	0.18	0.22	0.18	67.2	52.0	56.3	76.8	252

SN Zwicky													
$\eta$ (slope)	$\kappa$ (convergence)				$\gamma$ (shear)				$\mu$ (macro magnification)				
	A	B	C	D	A	B	C	D	A	B	C	D	$\Sigma$
2.10	0.74	0.31	0.62	0.32	0.85	0.41	0.72	0.42	1.55	3.33	2.68	3.60	11.2
2.05	0.73	0.35	0.62	0.36	0.78	0.40	0.67	0.41	1.87	3.78	3.23	4.08	13.0
2.00	0.72	0.38	0.63	0.39	0.72	0.38	0.63	0.39	2.24	4.28	3.87	4.63	15.0
1.95	0.72	0.42	0.64	0.43	0.67	0.37	0.59	0.38	2.69	4.89	4.63	5.29	17.5
1.90	0.73	0.45	0.65	0.46	0.62	0.35	0.55	0.36	3.21	5.60	5.52	6.06	20.4
1.85	0.73	0.48	0.66	0.49	0.58	0.34	0.52	0.34	3.85	6.47	6.60	7.01	23.9
1.80	0.74	0.52	0.67	0.52	0.53	0.32	0.48	0.32	4.65	7.55	7.93	8.18	28.3
1.75	0.75	0.55	0.69	0.55	0.49	0.30	0.45	0.31	5.58	8.79	9.47	9.53	33.4
1.70	0.76	0.58	0.71	0.59	0.45	0.28	0.42	0.29	6.78	10.4	11.5	11.3	40.0
1.65	0.78	0.61	0.72	0.62	0.41	0.27	0.39	0.27	8.28	12.4	14.0	13.5	48.2
1.60	0.79	0.64	0.74	0.65	0.38	0.25	0.35	0.25	10.2	15.0	17.2	16.3	58.7
1.55	0.80	0.67	0.76	0.68	0.34	0.23	0.32	0.23	12.7	18.3	21.2	19.9	72.1
1.50	0.82	0.70	0.78	0.71	0.31	0.21	0.29	0.21	16.2	22.8	26.9	24.8	90.7
1.45	0.84	0.73	0.80	0.74	0.27	0.19	0.26	0.19	20.7	28.6	34.2	31.2	115
1.40	0.85	0.76	0.82	0.77	0.24	0.17	0.23	0.17	27.4	37.2	44.9	40.6	150

### 3.4. Mass slope constraints from standard candle magnifications

Constraining the mass slope  $\eta$  of the lens galaxy from photometric observations alone is challenging, particularly for SN Zwicky, which occurred at an offset of 7 kpc from its host galaxy’s centre and therefore lacks strongly lensed host galaxy arcs. This is not an uncommon scenario; around half of strongly lensed SNe is expected to be without a strongly lensed host (Sainz de Murieta et al. 2024). An alternative approach for constraining the mass slope is to utilise the standard candle nature of SNIa, which provides information about the absolute magnification. The magnification of the macro lensing model,  $\mu_{\text{th}}$ , depends strongly on the slope of the mass profile, with flatter profiles providing larger magnifications. However, constraining the mass slope through the observed magnification can only be done when the additional magnification effects of microlensing are taken into consideration. Section 4 describes our approach to modelling microlensing effects through simulations, which require inputs for the convergence ( $\kappa$ ) and shear ( $\gamma$ ). We use observations from the Keck  $J$ -band to model the lens systems of iPTF16geu and SN Zwicky, and determine the  $\kappa$  and  $\gamma$  values for each SN image, for a range of mass

slopes between  $\eta = 1.4$  and  $\eta = 2.1$  (step size 0.05). Our range of  $\eta$  values was initially chosen to encompass the most common slope values from known lens galaxies, and eventually extended to lower  $\eta$  values to capture the 95% confidence level contours for iPTF16geu and SN Zwicky. We also compute the predicted macro magnification  $\mu_{\text{th}}$  for each SN image and slope value, which, in combination with the simulated microlensing magnification distributions, allows us to determine the best-fit slope values of iPTF16geu and SN Zwicky. Table 1 shows the best-fit convergence, shear and magnification values per slope and per image for SN Zwicky and iPTF16geu, and Fig. 3 shows results and residuals of SN Zwicky’s best-fit macrolens model for a slope of  $\eta = 1.8$ .

### 4. MICROLENSING SIMULATIONS

In order to incorporate the effects of microlensing at the SN image positions for both SN Zwicky and iPTF16geu, we simulate microlensing magnification maps. The three main parameters that govern the microlensing maps are the convergence (projected surface mass density),  $\kappa$ , the shear,  $\gamma$ , and the compact object fraction,  $f_c$ . From the macro lens model fits described in section 3, we estimate the best-fit  $\kappa$  and  $\gamma$  values for each SN image and each mass slope (with  $\eta$  ranging from 1.4

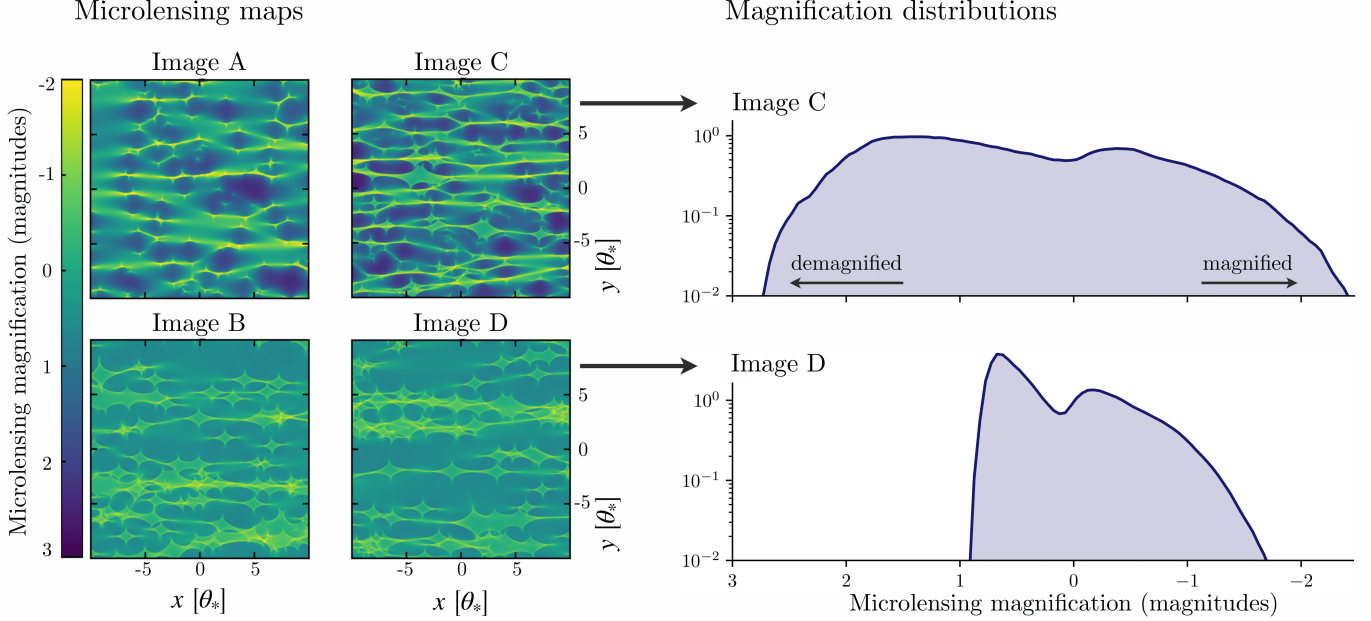


FIG. 4.—: Microlensing magnification maps and distributions for SN Zwicky, assuming a lens mass slope  $\eta = 1.8$  and compact object fraction  $f_c = 0.2$ . The microlensing magnification is given in units of magnitudes,  $\Delta m = -2.5 \log_{10}(\mu_{\text{obs}}/\mu_{\text{th}})$ . *Left:* Microlensing magnification maps for images A, B, C, and D. The microlensing caustics show the areas of magnification and demagnification in the source plane due to compact objects in the lens galaxy.  $\theta_*$  refers to the Einstein radius of an individual microlens. *Right:* The magnification distributions for images C and D, obtained by convolving the SN size with the microlensing maps. The microlensing magnification distributions for images A and C are similar and show a wide spread in magnifications, since they are both saddle points in the time-delay surface. Images B and D show similarly narrow distributions, because they represent minima in the time-delay surface.

to 2.1; see Table 1). For our range of  $\eta$  values and for  $f_c$  ranging from 0.1 to 1.0 in steps of 0.1, we create magnification maps for all four lensed SN images. An example of the resulting microlensing magnification maps and distributions for SN Zwicky with  $\eta = 1.8$  and  $f_c = 0.2$  is displayed in Fig. 4.

The microlensing magnification maps are created using Inverse Polygon Mapping (Mediavilla et al. 2006; Jiménez-Vicente & Mediavilla 2022) implemented on a GPU for efficiency (Weisenbach 2025). The maps are 20 Einstein radii and 10,000 pixels per side. This is a large enough size to create a representative magnification distribution (Vernardos & Fluke 2013), while the pixel scale corresponds to approximately 1 day of SN expansion. The maps are convolved with a uniform disk to approximate the size and profile of the expanding SN photosphere at observation, a sufficient approximation for our purposes (Pierel & Rodney 2019). While more complex SN intensity models may formally be more accurate (Goldstein et al. 2018; Huber et al. 2019), the main source parameter that impacts microlensing is the half-light radius of the source (Mortonson et al. 2005; Vernardos & Tsagkatakis 2019). For both iPTF16geu and SN Zwicky, the size of the photosphere at the time of observations is of the order of a light day. We average 10 maps for the final microlensing magnification probability distributions in order to minimize scatter from simulating a finite source plane region.

The maps are created using a single mass (in our case,  $1M_\odot$ ) for all the microlenses, a common approximation as the magnification distribution is largely insensitive to

a mass spectrum, except in extreme scenarios (Schechter et al. 2004). We note that the precise value of the mass used only loosely effects results, as the SN is still only a fraction of an Einstein radius in size, and a smaller microlens mass is degenerate with a larger source size (higher SN expansion speed). The number of microlenses used to create each map depends on the macro-model parameters, but is large enough to ensure that the majority of microlensed flux is accounted for (Katz et al. 1986).

## 5. STELLAR MASS AND LIGHT INFERENCE

We derive estimates of the stellar mass fractions at the image positions for SN Zwicky and iPTF16geu, based on photometric observations taken when the SNe were active, and after they had faded away. To obtain the stellar mass fractions, we require estimates of the total stellar mass of the lens galaxies, along with the total flux and the flux density at the image positions, which allow us to scale the stellar mass to the image positions. Finally, we divide this by the total mass density at the image positions, obtained from the lens modelling, to get the stellar mass fractions at the SN image positions. This Section describes how we estimate the stellar masses and light models of the lens galaxies.

### 5.1. Lens galaxy stellar mass estimates

The lens galaxy stellar masses are inferred from a series of photometric observations in the visible and NIR, which are fitted with a spectral energy distribution (SED) model. We use `prospector` to fit an SED model based on flexible stellar population synthesis (FSPS; Conroy et al. 2009, 2010; Conroy & Gunn 2010; via the `python-fps`

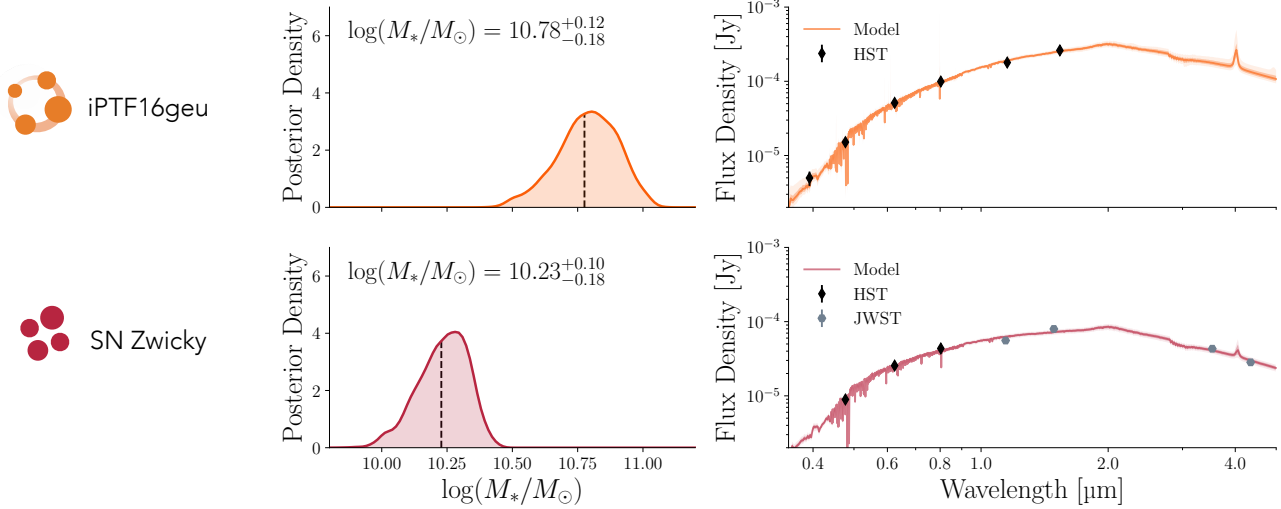


FIG. 5.—: Stellar mass estimates for iPTF16geu (top) and SN Zwicky (bottom) obtained with `prospector`. The left panels show the stellar mass posteriors, and the right panels the best-fit SEDs and photometric measurements used for the analysis. For iPTF16geu, the observations consist of six filters from *HST*, and for SN Zwicky, three filters from *HST* and four from *JWST*.

bindings; Johnson et al. 2024) to our photometric observations of the two lens galaxies. We infer the stellar mass ( $M_*/M_\odot$ ) jointly with the stellar metallicity ( $Z_*/Z_\odot$ ), optical depth of dust ( $\tau_{5500}$ ), and two parameters describing the star formation history ( $t_{\text{age}}$ ,  $\tau_{\text{SF}}$ ). Although the photometry alone does not constrain the additional parameters, we leave them free to get a robust estimate of the stellar mass uncertainty. We use the MILES stellar template library (Sánchez-Blázquez et al. 2006), MIST isochrones (Choi et al. 2016), a Chabrier (2003) initial mass function, and a parametric star formation history (SFH) that is linearly increasing at early times and exponentially decaying at late times (see e.g. Carnall et al. 2019; Johnson et al. 2021). The SFH has the form

$$\text{SFR}(t) \propto \frac{t_{\text{age}} - t}{\tau_{\text{SF}}} \times \exp\left(\frac{t - t_{\text{age}}}{\tau_{\text{SF}}}\right), \quad (4)$$

where  $t_{\text{age}}$  is the age of the galaxy,  $0 < t \leq t_{\text{age}}$  is look-back time, and  $t_{\text{age}} - \tau_{\text{SF}}$  sets the peak of the SFH. We use the Calzetti et al. (2000) dust attenuation law, with fixed slope and optical depth  $\tau_{5500}$  at 5500 Å. Gas-phase metallicity is coupled to stellar metallicity, with nebular emission being provided by the Cloudy (Ferland et al. 2013) model grids from Byler et al. (2017). We correct for Milky-Way dust using the Gordon et al. (2023) extinction curve (implemented in Gordon 2024, and relying on work from Gordon et al. 2009; Fitzpatrick et al. 2019; Gordon et al. 2021; Decleir et al. 2022) with  $R_V = 3.1$ , and  $E(B - V)$  estimated from the Schlafly & Finkbeiner (2011) dust map. We infer  $E(B - V) = 0.0725$  mag for iPTF16geu, and  $E(B - V) = 0.1558$  mag for SN Zwicky. We carry out our inference with the lens galaxy redshifts fixed.

The posterior distribution over our five model parameters is sampled using a dynamic nested sampler (Skilling 2004, 2006; Higson et al. 2019) implemented in `dynesty` (Speagle 2020; Koposov et al. 2024), with a proposal strategy based on rejection sampling within ellipsoidal bounds (Feroz et al. 2009). Our priors are:

$\log(M_*/M_\odot) \sim \mathcal{U}(8, 12)$ ,  $\log(Z_*/Z_\odot) \sim \mathcal{U}(-2.00, 0.19)$ ,  $\tau_{5500} \sim \mathcal{U}(0, 2)$ ,  $t_{\text{age}}/\text{Gyr} \sim \mathcal{U}(0, t_{\text{Univ}}(z))$ , and  $\log(\tau_{\text{SF}}/\text{Gyr}) \sim \mathcal{U}(-1, \log(30))$ . Fig. A.1 in the Appendix shows a corner plot of all the free parameters used in the stellar mass fits for iPTF16geu and SN Zwicky.

### 5.1.1. iPTF16geu stellar mass

To estimate the stellar mass of iPTF16geu’s lens galaxy, we use reference observations in the  $F390W$ ,  $F475W$ ,  $F625W$ ,  $F814W$ ,  $F110W$ , and  $F160W$  bands from *HST*, taken after the SN faded away. We compute the photometry within an aperture with radius 1'' on the lens galaxy centre. Measuring the photometry for iPTF16geu is complicated by the fact that the lens galaxy is blended with the lensed arcs from the host galaxy. To separate the light contributions from the lens and the host galaxy, we simultaneously model the  $F475W$ ,  $F625W$ , and  $F814W$  filters from *HST*, following the approach outlined in section 3. In each filter, we compute the fraction of the flux coming from the lens galaxy inside the 1'' aperture, and multiply that with the photometry measurements. The lens and host galaxy are difficult to disentangle in the *HST*  $F110W$  and  $F160W$  bands, and therefore, we use the Keck  $J$ -band observation to estimate the lens galaxy flux fraction in the NIR. Details about the iPTF16geu Keck  $J$ -band light modelling are given in section 5.2. The photometry and lens fraction measurements in all filters are given in Table 2. The resulting stellar mass estimate for iPTF16geu’s lens galaxy is  $\log(M_*/M_\odot) = 10.78^{+0.12}_{-0.18}$ , for which the full stellar mass posterior and the best-fit SED from `prospector` are shown in Fig. 5.

### 5.1.2. SN Zwicky stellar mass

For SN Zwicky, the input for `prospector` are *HST* observations in the  $F475W$ ,  $F625W$ , and  $F814W$  bands, and *JWST* observations in the  $F115W$ ,  $F150W$ ,  $F356W$ , and  $F444W$  bands, all taken after the SN faded away. In this case, the analysis of the lens galaxy is aided by the fact that the host galaxy is not strongly lensed

TABLE 2: Photometry and lens fraction measurements for iPTF16geu and SN Zwicky, which serve as input for the stellar mass analysis with `prospector`. The lens fraction is the ratio between the lens galaxy flux and the total flux. Both the photometry and lens fractions are measured within an aperture with radius  $1''$ . For iPTF16geu, observations in six *HST* filters are used. For SN Zwicky, *HST* observations in the  $F475W$ ,  $F625W$ , and  $F814W$  bands, and *JWST* observations in the  $F115W$ ,  $F150W$ ,  $F356W$ , and  $F444W$  filters are used. We also quote the Milky Way extinction correction (in magnitudes) for each band, computed using the [Gordon et al. \(2023\)](#) curve. The photometric measurements are given in AB magnitudes, and have not been corrected for Milky-Way reddening or the lens fractions.

#### iPTF16geu lens galaxy photometry (*HST*/WFC3)

	$F390W$	$F475W$	$F625W$	$F814W$	$F110W$	$F160W$
Photometry	$22.46 \pm 0.24$	$21.08 \pm 0.12$	$19.55 \pm 0.06$	$18.68 \pm 0.05$	$17.82 \pm 0.05$	$17.27 \pm 0.05$
Lens fraction	0.980	0.880	0.780	0.720	0.620	0.560
MW extinction	0.320	0.267	0.191	0.130	0.068	0.042

#### SN Zwicky lens galaxy photometry (*HST*/WFC3 + *JWST*/NIRCam)

	$F475W$	$F625W$	$F814W$	$F115W$	$F150W$	$F356W$	$F444W$
Photometry	$22.03 \pm 0.05$	$20.68 \pm 0.06$	$20.00 \pm 0.08$	$19.34 \pm 0.10$	$18.98 \pm 0.10$	$19.57 \pm 0.10$	$19.79 \pm 0.10$
Lens fraction	0.944	0.904	0.927	0.727	0.784	0.786	0.630
MW extinction	0.573	0.410	0.279	0.148	0.095	0.021	0.016

and is located at a relatively large distance from the centre of the lens galaxy ( $\sim 1.4''$ ). We compute the flux within an aperture of radius  $1''$  (which excludes most of the host galaxy contribution) as input for `prospector`. To correct for small contributions of host galaxy flux, we model the lens and host galaxy to determine the lens galaxy flux fraction within the  $1''$  aperture. The photometric measurements and lens galaxy flux fractions are listed in Table 2. The resulting stellar mass estimate for SN Zwicky’s lens galaxy is  $\log(M_*/M_\odot) = 10.23^{+0.10}_{-0.18}$ , for which the full posterior and the best-fit SED from `prospector` are shown in Fig. 5.

#### 5.2. Lens galaxy light model for iPTF16geu

To model the lens galaxy light of iPTF16geu, we use Keck  $J$ -band observations of when the SN was active, as well as a reference observation after it had faded away. The Keck data provides the most detailed view of the lens galaxy’s light, with the NIR  $J$ -band selected for its ability to trace the older, redder stellar population that contributes the most to the stellar mass. While Keck observations in the  $H$  and  $K$  bands are also available, the SN images are not clearly visible in those bands, preventing the extraction of an accurate PSF to conduct the lens modelling.

We model the lens system as described in section 3.3. Additionally, we include a uniform residual background surface brightness layer with the lens light model to prevent background over- or under-subtraction. We simultaneously fit the reference observation and the observation with the active SN. This fitting choice enforces that the lens galaxy mass distribution, the lens galaxy light profile, and the host galaxy light profile are each consistent across the two epochs. Because the host galaxy is faint in both observations, fitting the data jointly better constrains the model parameters. We carry out our analysis with a fixed lens galaxy mass slope of  $\eta = 1.8$ , after ensuring that this value does not impact the final lens light predictions. The resulting model of the reference image is shown in Fig. 6. We find that the Einstein radius is consistent with previous estimates of this parameter for iPTF16geu. To compute the flux densities at the SN image positions, we compare the lens light model flux at

the position of each image to the total flux from the lens light model within an aperture of  $1''$  radius from the lens galaxy centre.

#### 5.3. Lens galaxy light model for SN Zwicky

To construct the light model for SN Zwicky’s lens galaxy, we use *JWST* observations made by NIRCam in the  $F115W$  band. The observations were taken one year after the appearance of SN Zwicky, and hence the SN images are not visible anymore. In order to estimate the positions of the SN images on the lens galaxy, we use the *HST*  $F814W$  band observations from when SN Zwicky was active. We combine the observations by projecting the *HST* data of SN Zwicky on top of the *JWST* observations using the publicly available software `reproject`<sup>4</sup> ([Robitaille et al. 2020](#)). The projection is done through the World Coordinate Systems of both observations. We correct remaining shifts between the observations by fitting five stars in the field with a Moffat profile and correcting for their offsets. To ensure the clearest representation of SN Zwicky’s image positions, we use the difference image between *HST*’s observations with the active SN and the reference observations taken a year later. Fig. 1 shows the *JWST* data with the projected SN Zwicky image positions. Finally, we fit a Moffat profile to the projected SN images to accurately determine their positions within the *JWST* observation.

To estimate the lens galaxy flux at the image positions, we focus on the light profile in the centre of the lens galaxy, where the SN images are located. Therefore, we model the lens galaxy light within a square window of side length ( $0.6'', 0.6''$ ) around the lens galaxy with a double Sérsic profile (Eq. 2), convolved with a Gaussian PSF with full width at half maximum  $0.04''$ , obtained from fitting a star in the field. We experimented with using a Moffat PSF and a cut-out of a star in the field, but the Gaussian PSF gave the best fit and smallest residuals for this smaller patch. After modelling, the image flux densities are computed by evaluating the lens light model at the projected SN image positions. The total lens galaxy flux corresponding to the stellar mass

<sup>4</sup> <https://reproject.readthedocs.io/en/stable/>

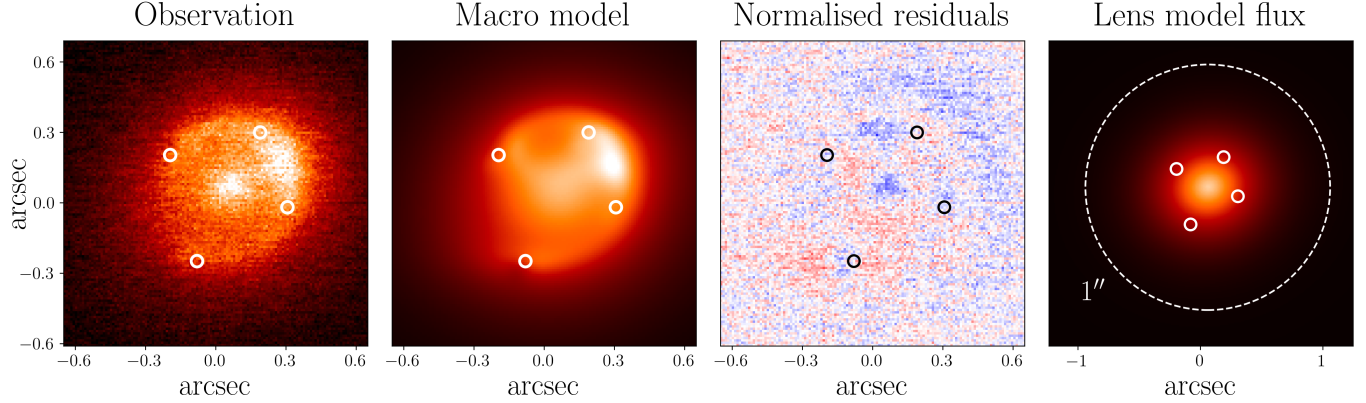


FIG. 6.—: Lens light modelling of iPTF16geu using Keck observations in the  $J$ -band, with the SN image positions projected as white/black open circles. From left to right: the reference observation of the lens and host galaxy, the best-fit macro model, normalised residuals, and the lens light model. To infer the stellar mass at the image positions, the stellar mass to light ratio is computed using the total flux in an aperture of  $1''$ , which is scaled with the flux density at the SN image positions.

estimate is computed by summing the lens galaxy flux within a  $1''$  radius from the lens centre.

For both iPTF16geu and SN Zwicky, we determine the stellar mass-to-light ratios by dividing their stellar mass estimates by the lens galaxy flux within the same aperture. We multiply the image position’s flux densities with the stellar mass-to-light ratio to obtain the stellar surface mass density at the image positions. By dividing the stellar surface mass densities by the total surface mass densities ( $\kappa$  obtained from the lens modelling), we obtain the stellar mass fractions at the image positions. In practice, the inferred stellar masses, fluxes, and flux densities are used as inputs in our joint Bayesian model to constrain the mass slopes and fraction of compact objects, as described in section 6. More details about the stellar mass fraction calculation are given in section 6.3.

## 6. BAYESIAN MODEL

In this section, we introduce our Bayesian model to infer the lens galaxy mass slope,  $\eta$ , and dark compact object fraction,  $f_{dc}$ , based on quantities derived from the photometric observations, which have been described in the previous sections. The following subsections describe the observables, free parameters, derived parameters, the posterior, likelihood, priors, and inference method. A probabilistic graphical model summarising the parameters of interest and their connections is displayed in Fig. 7.

### 6.1. Observed quantities

The photometric observations of SN Zwicky and iPTF16geu have been reduced to the following observed quantities. In all cases, a hat corresponds to an observed quantity, and a subscript  $i$  refers to the quantity evaluated for SN image  $i$ .

#### Observed quantities with uncertainties

- **Observed lens galaxy stellar mass  $\hat{M}_*$ :** as described in section 5.1, we used photometric observations and SED modelling to infer the stellar masses of the lens galaxies within an aperture of  $1''$  for iPTF16geu and SN Zwicky. The resulting estimates

are  $\log M_*/M_\odot = 10.78^{+0.12}_{-0.18}$  for iPTF16geu and  $\log M_*/M_\odot = 10.23^{+0.10}_{-0.18}$  for SN Zwicky.

- **Observed total magnification  $\hat{\mu}$ :** the observed magnification is determined by comparing the observed apparent magnitudes of the lensed SNe with the expected magnitude of a standard SNIa at that redshift. We take the results for the total magnification (sum of all images) from Dhawan et al. (2020) for iPTF16geu,  $\hat{\mu} = 67.8 \pm 2.9$ , and from Goobar et al. (2023) for SN Zwicky,  $\hat{\mu} = 23.7 \pm 3.2$ .

#### Observed quantities as fixed inputs

The following observed quantities are treated as fixed inputs in the Bayesian model, as their uncertainties are negligible relative to other sources of uncertainty. The uncertainties in the lens galaxy flux and flux density are negligible in comparison to the uncertainty of the stellar mass estimate. Similarly, the image flux ratio uncertainties are negligible compared to the uncertainty on the total magnification.

- **Lens galaxy flux  $\hat{F}_{\text{lens}}$ :** the total lens light flux within an aperture of  $1''$ , as described in Sections 5.2 and 5.3.
- **Lens galaxy flux density at image positions  $\hat{S}_{\text{lens},i}$ :** the flux density at the SN image positions, obtained from the lens light model. Described in Sections 5.2 and 5.3
- **SN image flux ratios  $\hat{R}_i$ :** the observed flux ratios of the SN images, normalised to one. We take the results from Dhawan et al. (2020) for iPTF16geu,  $\hat{R}_i = [0.52, 0.23, 0.11, 0.13]$ , and from Goobar et al. (2023) for SN Zwicky,  $\hat{R}_i = [0.37, 0.15, 0.30, 0.18]$ .

## 6.2. Free parameters

The following parameters are sampled by the MCMC to obtain their posterior distributions. We expand on their priors in section 6.6.

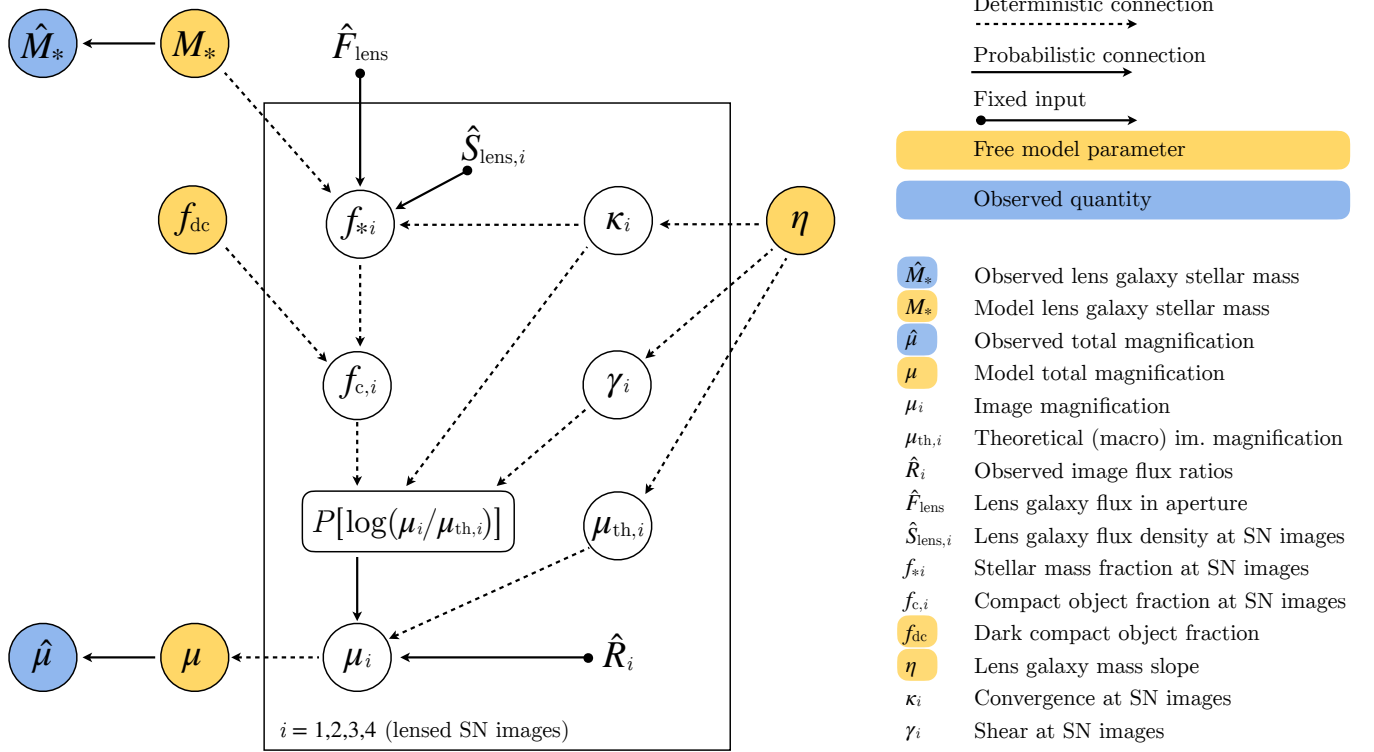


FIG. 7.—: Probabilistic graphical model for the Bayesian analysis, depicting the connections between the free parameters (yellow shaded:  $M_*$ ,  $\mu$ ,  $\eta$ ,  $f_{\text{dc}}$ ), the observables with uncertainties (blue shaded:  $\hat{M}_*$  and  $\hat{\mu}$ ), and the observables treated as fixed inputs ( $\hat{F}_{\text{lens}}$ ,  $\hat{S}_{\text{lens},i}$  and  $\hat{R}_i$ ). The arrows indicate relations of conditional probability, with solid arrows representing probabilistic connections and dashed ones deterministic connections. Parameters within the box, labelled  $i = 1, 2, 3, 4$ , are repeated for every lensed SN image, whereas parameters outside the box describe the total lensed SN system.

- **Lens galaxy mass slope  $\eta$ :** logarithmic slope of the lens galaxy's mass profile.
- **Fraction of dark compact objects  $f_{\text{dc}}$ :** the fraction of the lens galaxy's total mass that is in the form of dark compact objects. In our analysis, we assume a constant  $f_{\text{dc}}$  for each of the SN image positions, a reasonable approximation because the images are formed at similar radii from the lens galaxy centre.
- **Lens galaxy stellar mass  $M_*$ :** the true stellar mass of the lens galaxy, which the model aims to infer. It serves as the underlying quantity that generates the observed stellar mass,  $\hat{M}_*$ , through the likelihood function, accounting for observational uncertainties.
- **Total magnification  $\mu$ :** the true total magnification of the lensed SN system. It is the intrinsic quantity that generates the observed total magnification,  $\hat{\mu}$ , through the likelihood function, incorporating measurement uncertainties.

### 6.3. Derived parameters

In this section, we describe the derived parameters, which are quantities calculated from combinations of the observables and free parameters.

- **Stellar mass fractions  $f_{*,i}$ :** the fraction of the lens galaxy's total mass that is in the form of stars, at the

position of SN image  $i$ . Below, we describe how we calculate  $f_{*,i}$  from  $M_*$ ,  $\eta$ ,  $\hat{F}_{\text{lens}}$  and  $\hat{S}_{\text{lens},i}$ .

From the lens galaxy's stellar mass,  $M_*$ , and flux measurement within the same aperture,  $\hat{F}_{\text{lens}}$ , the stellar mass-to-light ratio,  $ML_*$ , can be determined:

$$ML_* = M_* / \hat{F}_{\text{lens}}. \quad (5)$$

Combined with the lens galaxy flux density at the SN image positions,  $\hat{S}_{\text{lens},i}$ , the stellar mass surface density at the images can be calculated:

$$\Sigma_{*,i} = ML_* \cdot \hat{S}_{\text{lens},i}, \quad (6)$$

which can be converted into a stellar critical surface density, or stellar convergence,  $\kappa_*$ :

$$\kappa_* = \Sigma_* \frac{4\pi G D_{\text{ds}} D_{\text{d}}}{c^2 D_s}, \quad (7)$$

with  $G$  the gravitational constant,  $c$  the speed of light, and  $D_{\text{l}}$ ,  $D_{\text{s}}$  and  $D_{\text{ls}}$  the angular diameter distances between the observer and the lens, the observer and the source, and the lens and the source, respectively. Distances are calculated using a standard flat  $\Lambda$ CDM model with  $H_0 = 67.4 \text{ km s}^{-1} \text{Mpc}^{-1}$  and  $\Omega_m = 0.315$  (Planck Collaboration et al. 2020). Finally, the stellar mass fraction is given by

$$f_{*,i} = \kappa_{*,i} / \kappa_i \quad (8)$$

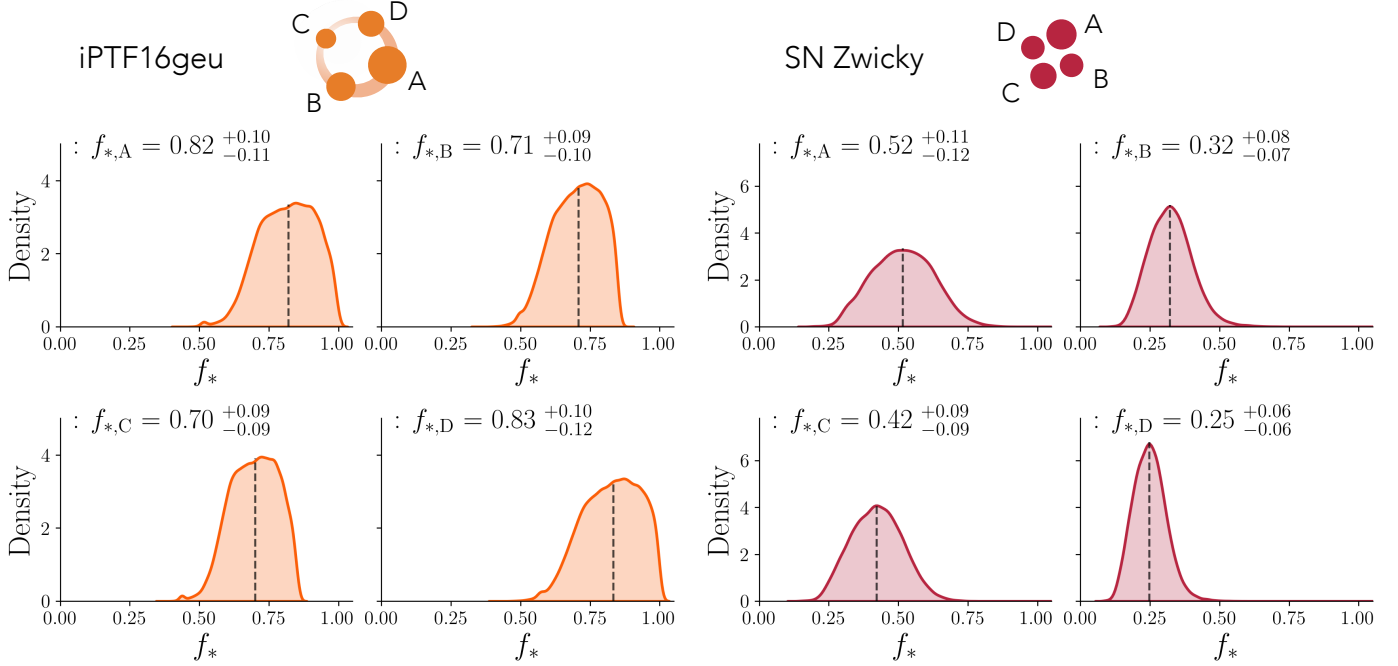


FIG. 8.—: Posteriors for the stellar mass fraction  $f_{*,i}$  at the image positions, for iPTF16geu (left) and SN Zwicky (right). The dashed line represents the median of the distribution, which is quoted above along with the 16th and 84th percentiles as uncertainties.

where  $\kappa_i$  is the total convergence for image  $i$ , calculated for different slope values as detailed in section 3 and in Table 1.

- **Fractions of compact objects  $f_{c,i}$ :** the lens galaxy's total mass fraction of compact objects at the SN image positions:  $f_{c,i} = f_{*,i} + f_{dc}$ .
- **Convergence  $\kappa_i$  and shear  $\gamma_i$ :** the surface mass density (convergence) and shear at the SN image positions. As described in section 3, we constrain the best-fit  $\kappa_i$  and  $\gamma_i$  values for a range of different mass slopes ( $\eta$  ranging from 1.4 to 2.1 in steps of 0.05), which are displayed in Table 1.
- **Predicted macro magnification per image  $\mu_{th,i}$ :** the magnification predicted by the best-fit macro lens model, at the SN image positions for a range of different mass slopes ( $\eta$  ranging from 1.4 to 2.1 in steps of 0.05). Described in more detail in section 3.
- **Magnification per image  $\mu_i$ :** the combined macro + microlensing magnification for each SN image.  $\mu_i$  is computed from the total magnification  $\mu$  and the SN image flux ratios  $\hat{R}_i$  as follows:  $\mu_i = \mu \hat{R}_i$ .

#### 6.4. The posterior

The posterior distribution provides the probabilistic constraints on the model parameters  $M_*$ ,  $\mu$ ,  $\eta$  and  $f_{dc}$ , given the observed quantities  $\hat{M}_*$ ,  $\hat{\mu}$ ,  $\hat{F}_{lens}$ ,  $\hat{S}_{lens,i}$  and  $\hat{R}_i$ . This distribution is defined by Bayes' theorem as the product of the likelihood and the prior terms, and can

be expressed as follows:

$$\begin{aligned} P(M_*, \mu, \eta, f_{dc}, | \hat{M}_*, \hat{\mu}, \hat{F}_{lens}, \hat{S}_{lens,i}, \hat{R}_i) &\propto \\ P(\hat{\mu} | \mu) P(\hat{M}_* | M_*) P(\mu | M_*, \eta, f_{dc}, \hat{F}_{lens}, \hat{S}_{lens,i}, \hat{R}_i) \\ P(M_*, \eta, f_{dc} | \hat{F}_{lens}, \hat{S}_{lens,i}) \end{aligned} \quad (9)$$

The likelihood and prior terms on the right-hand-side are described in more details below.

#### 6.5. Likelihoods on data

The likelihood terms in the posterior distribution quantify how well the proposed model parameters explain the observed data.

•  **$P(\hat{M}_* | M_*)$ .** The observed stellar mass,  $\hat{M}_*$ , represents the stellar mass of the lens galaxy inferred within an aperture of  $1''$ . As detailed in section 5.1, the summaries of our stellar mass estimates are  $\log M_*/M_\odot = 10.78^{+0.12}_{-0.18}$  for iPTF16geu and  $\log M_*/M_\odot = 10.23^{+0.10}_{-0.18}$  for SN Zwicky. To incorporate the observed stellar mass into our inference model, we construct a kernel density estimate (KDE) of the stellar mass measurements. The likelihood  $P(\hat{M}_* | M_*)$  is then evaluated by computing the probability density of the proposed stellar mass  $M_*$  using the KDE.

•  **$P(\hat{\mu} | \mu)$ .** The observed total magnification,  $\hat{\mu}$ , is determined by comparing the apparent magnitudes of the lensed SNe with the expected magnitudes of standard SNe Ia at the same redshifts. For iPTF16geu, we adopt the value  $\hat{\mu} = 67.8 \pm 2.9$  from [Dhawan et al. \(2020\)](#). For SN Zwicky, we use  $\hat{\mu} = 23.7 \pm 3.2$  from [Goobar et al. \(2023\)](#). The likelihood  $P(\hat{\mu} | \mu)$  is modelled as

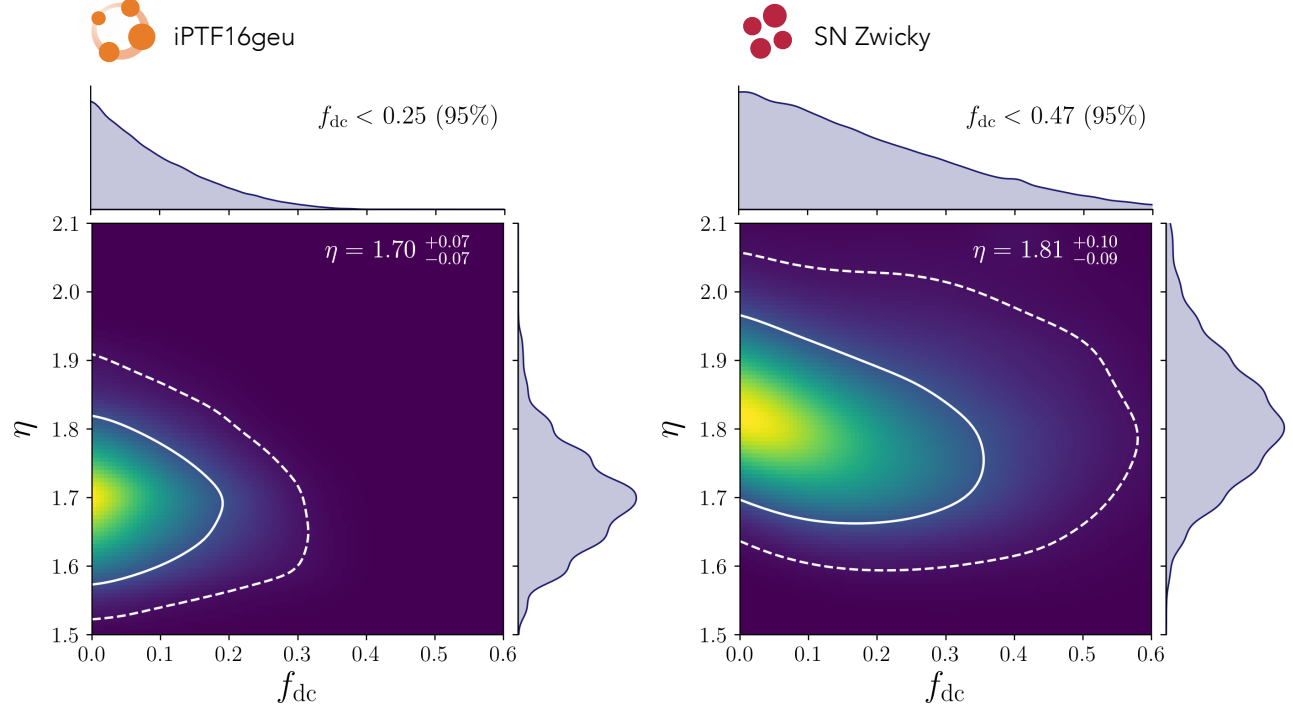


FIG. 9.—: The joint probability of the galaxy mass slope,  $\eta$ , and the dark compact object fraction,  $f_{\text{dc}}$ , derived from the observations of iPTF16geu (left) and SN Zwicky (right). The solid and dashed contours correspond to the 68% and 95% confidence intervals, respectively.

a Gaussian distribution with mean and standard deviation equal to the reported values in the respective studies.

#### 6.6. Priors

The prior on the total magnification,  $\mu$ , is derived from the simulated microlensing magnification distributions. These distributions are evaluated for each SN image at its magnification,  $\mu_i = \mu \hat{R}_i$ , and combined multiplicatively across all images:

$$P(\mu | M_*, \eta, f_{\text{dc}}, \hat{F}_{\text{lens}}, \hat{S}_{\text{lens},i}, \hat{R}_i) = \prod_{i=1}^N P(\mu \hat{R}_i | M_*, \eta, f_{\text{dc}}, \hat{F}_{\text{lens}}, \hat{S}_{\text{lens},i}), \quad (10)$$

where  $P(\mu \hat{R}_i | M_*, \eta, f_{\text{dc}}, \hat{F}_{\text{lens}}, \hat{S}_{\text{lens},i})$  is the microlensing magnification distribution for image  $i$  evaluated at  $\mu_i = \mu \hat{R}_i$ . In practice, the total magnification  $\mu$  is sampled from a uniform proposal distribution,  $\mathcal{U}(\mu; 15, 50)$ , and multiplied by the SN image flux ratios  $\hat{R}_i$  to obtain  $\mu_i$ . For the remaining free parameters, we use the following priors:

$$P(M_*, \eta, f_{\text{dc}} | \hat{F}_{\text{lens}}, \hat{S}_{\text{lens},i}) = P(f_{\text{dc}} | M_*, \eta, \hat{F}_{\text{lens}}, \hat{S}_{\text{lens},i}) P(M_*) P(\eta), \quad (11)$$

with

$$P(f_{\text{dc}} | M_*, \eta, \hat{F}_{\text{lens}}, \hat{S}_{\text{lens},i}) = \prod_{i=1}^N \mathcal{U}(f_{\text{dc}} + f_{*,i}; 0, 1). \quad (12)$$

The prior in eq. 12 ensures that for each SN image, the fraction of compact objects  $f_{c,i} = f_{\text{dc}} + f_{*,i}$  is between 0 and 1. For  $P(M_*)$  and  $P(\eta)$ , we initialise the walkers in a range of  $\mathcal{U}(M_*; 10^9, 10^{10.8})$  and  $\mathcal{U}(\eta; 1.4, 2.1)$ , and we have uninformative priors over the entire parameter space. The values of  $\eta$  are sampled from a continuous distribution but are rounded to the nearest 0.05 to match the precision used in the microlensing simulations. Similarly, the compact object fraction per image,  $f_{c,i} = f_{\text{dc}} + f_{*,i}$  is rounded to the nearest 0.1 to align with the simulation's precision.

#### 6.7. Inference

We sample the posteriors of our parameters of interest using `emcee`. This approach allows us to incorporate observational uncertainties, apply prior constraints to the model parameters, and sample the parameters of interest jointly to assess their covariances. `emcee` is able to handle a combination of continuous and discrete parameters effectively, since it does not rely on gradient information to propose new states. This is particularly useful in our situation, where we have a discrete number of microlensing magnification distributions, corresponding to discrete values of  $\eta$  and the compact object fraction per image.

We run MCMC chains with 100 walkers and 3000 iterations to sample  $\eta$ ,  $f_{\text{dc}}$ ,  $M_*$ , and  $\mu$ . We verify the convergence of the chains by inspecting the trace plots. After discarding the first 500 samples for the burn-in phase, we combine the chains to derive the marginalized posterior distributions for each parameter, from which we report the median values and the corresponding 16th and 84th percentiles as uncertainties. Our results are summarised in the next Section.

## 7. RESULTS

In this section, we present the main results obtained from the parameter inference model outlined in section 6.

### 7.1. Stellar mass fractions

The stellar mass fraction of the lens galaxy at the SN image positions,  $f_{*,i}$ , is a derived parameter in our model, calculated from the stellar mass,  $M_*$ , the lens galaxy flux,  $\hat{F}_{\text{lens}}$ , the lens galaxy flux density at the SN image positions,  $\hat{S}_{\text{lens},i}$ , and the convergence at the image positions,  $\kappa_i$ . Fig. 8 shows the inferred stellar mass fractions per lensed SN image, for iPTF16geu and SN Zwicky. Both iPTF16geu and SN Zwicky have high stellar mass fractions, which can be explained by the fact that the SN images are formed close to the lens centre, where the stellar density is high compared to the dark matter density. The median  $f_{*,i}$  values for iPTF16geu ( $\sim 0.7 - 0.8$ ) are higher than the ones inferred for iPTF16geu in Mörtsell et al. (2020) ( $\sim 0.2$ ), which is due to differences in the stellar mass determination between the papers. In Mörtsell et al. (2020), the stellar mass was inferred from scaling relations in Kauffmann et al. (2003), whereas in this work, we model the full lens galaxy SED with `prospector`.

### 7.2. Dark compact objects and galaxy mass slopes

Fig. 9 shows the joint  $\eta$  and  $f_{\text{dc}}$  posterior distributions for iPTF16geu and SN Zwicky. For both lensed SNe, there is no preference for additional dark compact objects, and stars alone are sufficient to explain the observed microlensing effects. We put upper limits at the 95% confidence level on the fraction of dark compact objects of  $f_{\text{dc}} < 0.25$  for iPTF16geu and  $f_{\text{dc}} < 0.47$  for SN Zwicky. The upper limits from iPTF16geu are tighter than those from SN Zwicky, due to the fact that iPTF16geu has high stellar mass fractions ( $\sim 0.7 - 0.8$ ), leaving less room for the presence of dark compact objects. These limits apply to compact objects with masses greater than  $0.02M_{\odot}$ . Microlenses with lower masses have Einstein radii smaller than the size of the SN photosphere, causing their magnification contributions to average out.

By utilising the standard candle nature of SNIa, while incorporating microlensing into our modelling, we were able to constrain the galaxy mass slopes for these systems, which are difficult to infer from lens modelling alone. For iPTF16geu, we find a slope of  $\eta = 1.70 \pm 0.07$ , which is slightly lower but consistent with the value derived in Mörtsell et al. (2020) ( $\eta \sim 1.8$ ). SN Zwicky's mass slope is  $\eta = 1.81 \pm 0.10$ . The step-like features in the posterior distribution of  $\eta$  reflect the discreteness introduced by the microlensing simulations.

For the best-fit slope values, the microlensing magnification contributions for images A-D (in magnitudes) are the following:

iPTF16geu:  $-0.72, -0.05, 0.78, 0.97$  mag.

SN Zwicky:  $-0.68, 0.79, 0.10, 0.74$  mag.

For both iPTF16geu and SN Zwicky, the brightest observed images are  $\sim 0.7$  magnitudes brighter due to microlensing, which is in line with microlensing expectations for lensed SNe (Dobler & Keeton 2006), especially

considering those images are both saddle points, which are more strongly affected by microlensing.

In Fig. 10, we plot our inferred mass slopes for iPTF16geu and SN Zwicky together with those from lens galaxies in the Sloan Lens ACS Survey (SLACS; Auger et al. 2010) and in the Strong Lensing Legacy Survey (SL2S; Sonnenfeld et al. 2013), as a function of redshift and stellar mass. iPTF16geu and SN Zwicky's mass slopes are relatively low compared to the lens galaxy population, while still being within the range observed for other galaxies. In terms of stellar mass, SN Zwicky is significantly lighter than the other lens galaxies. As was pointed out in Goobar et al. (2023), iPTF16geu and SN Zwicky are the first discoveries of a new class of extremely low-mass and compact lens systems, identified primarily due to their high magnification. These discoveries were only possible because the lensed sources were SNIa with standardisable brightnesses. In this work, we have demonstrated that these lensing systems are highly suitable for microlensing studies and for constraining the matter in compact objects.

### 7.3. Shared $f_{\text{dc}}$ for iPTF16geu and SN Zwicky

If we make the assumption that the fraction of dark compact objects is the same across different galaxies, we can combine the constraints from iPTF16geu and SN Zwicky. This could be the case if the dark compact objects were all created in the very early Universe, and are spread evenly throughout the Universe and across galaxies. We performed another inference run with a joint Bayesian model, where the free parameters are  $f_{\text{dc}}$ ,  $\eta$  Zwicky,  $\log M_*$  Zwicky,  $\mu$  Zwicky,  $\eta$  iPTF16geu,  $\log M_*$  iPTF16geu, and  $\mu$  iPTF16geu. The data constraints we use are the same as in the individual fits. Fig. A.2 shows the resulting corner plots for all free parameters, where the results for  $\eta$  are consistent with the individual fits. We obtain a tighter upper bound on the fraction of dark compact objects:  $f_{\text{dc}} < 0.19$  at the 95% confidence level.

## 8. DISCUSSION AND CONCLUSION

In this work, we analysed the micro- and macro lens models of the two galaxy-scale lensed SNIa: iPTF16geu and SN Zwicky. Given that these systems both have standardizable candle sources that show strong hints of microlensing in their flux ratios – deviating from macro-model predictions – they are ideal to explore the potential of strongly lensed SNe for microlensing studies. We simulated realistic microlensing magnification distributions for a range of different galaxy mass slope values and compact object fractions. By doing so, we evaluated which combination of slope and compact objects is the most likely, and whether there are signs of a population of dark compact objects in the lens galaxy.

We developed a Bayesian model to simultaneously model our parameters of interest, taking into account constraints from observed quantities such as the stellar mass, magnification, lens galaxy light model, and SN image flux ratios. Our results show that there is no preference for additional dark compact objects in the lens galaxy, and we place 95% upper limits of  $f_{\text{dc}} < 0.25$  for iPTF16geu and  $f_{\text{dc}} < 0.47$  for SN Zwicky. Our results are in agreement with  $f_{\text{dc}}$  measurements from strongly lensed quasars, which also find no evidence for any dark

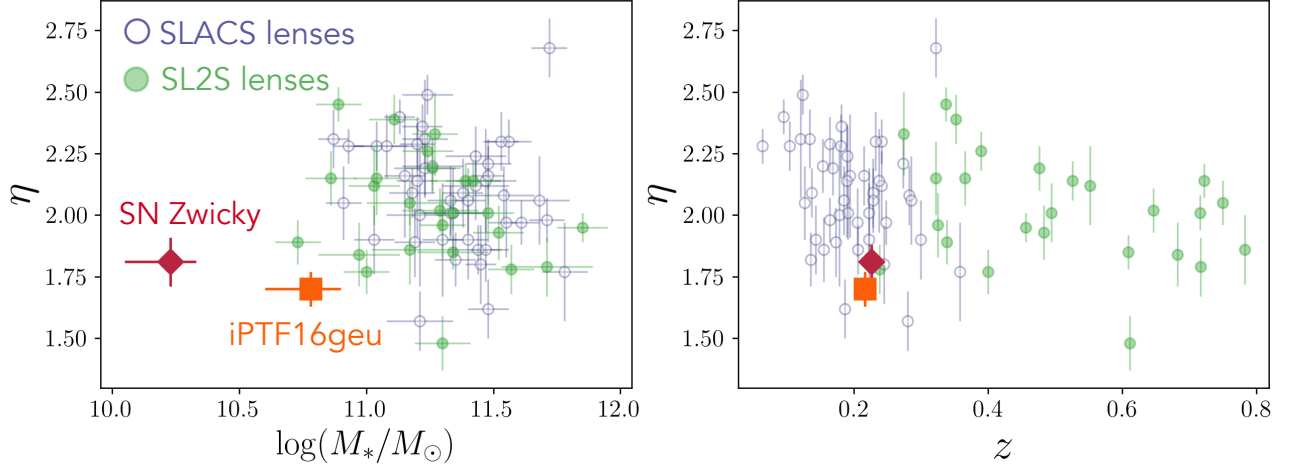


FIG. 10.—: Lens galaxy mass slope,  $\eta$ , versus stellar mass,  $M_*$ , (left panel) and redshift (right panel), for iPTF16geu, SN Zwicky, and several lensed galaxies from the SLACS (Auger et al. 2010) and SL2S (Sonnenfeld et al. 2013) surveys. The lens galaxies of iPTF16geu and SN Zwicky have relatively low stellar masses (see section 5.1) and flat mass profiles (see section 7) compared to the population of observed lensed galaxies.

compact objects (e.g. Pooley et al. 2009, 2012; Schechter & Wambsganss 2004; Schechter et al. 2014; Mediavilla et al. 2009, 2017; Esteban-Gutiérrez et al. 2020; Mediavilla & Jiménez-Vicente 2025). With a larger sample of lensed SNe Ia, we will eventually be able to test whether the initial mass function (assumed to be Chabrier in this work) is correct, as we become more sensitive to  $f_{dc}$ , or equivalently the stellar mass-to-light ratio (Weisenbach et al. 2025).

We also constrain the mass slope of the lens galaxies, which is made possible because they are standardizable candles for which we know their magnification. We measure  $\eta = 1.70 \pm 0.07$  for iPTF16geu and  $\eta = 1.81 \pm 0.10$  for SN Zwicky. Compared to other known lens galaxies from SLACS and SL2S, these slope measurements are on the lower side, but not outside of what has been observed before. For SN Zwicky, which does not have a lensed host galaxy, this measurement using the SNIa intrinsic brightness is the only way to place tight constraints on the mass slope. For iPTF16geu, we can cross-check this measurement with the one obtained by fitting a PEMD lens model with the slope as a free parameter, as is done in Mörtsell et al. (2020), which is in agreement.

We also investigated an alternative explanation for the observed flux ratio anomalies in iPTF16geu and SN Zwicky: angular complexity in the lens model. We tested lens models with fourth-order multipole perturbations and found that they cannot account for the observed flux ratios, leaving microlensing as the most likely cause.

Future work on microlensing of lensed SNe can take into account time varying microlensing effects, as well as a spectrum of different microlens masses. Additionally, in our work we did not consider the effects of *mililensing*, due to dark matter subhalos. The recent analysis of SN Zwicky by Larison et al. (2024), which included *HST* reference observations, investigated mililensing, and found its contribution to the total magnification to be negligible. Additionally, they investigated the flux ratio discrepancies of SN Zwicky in the  $F475W$ ,  $F625W$ ,  $F814W$ , and  $F160W$  filters, confirming the evidence for

microlensing and finding hints for a chromatic nature of the effects.

This work demonstrates the power of strongly lensed SNe to obtain insights into compact objects and potential primordial black hole populations. With the advance of the next generation of telescopes such as the Vera C. Rubin Observatory (Ivezic et al. 2019) and the Nancy Grace Roman Space Telescope (e.g., Pierel et al. 2021), we will discover dozens more galaxy-scale lensed SNe, which will allow us to put tighter constraints on the population of dark compact objects. Moreover, these compact lensed SN systems offer one of the few avenues to probe the inner mass slope of lower-mass lens galaxies.

#### ACKNOWLEDGMENTS

We are grateful to Simon Birrer and Anowar Shahib for helpful suggestions regarding the lens modelling of iPTF16geu. We would like to thank Jorge Martin Camalich and Evencio Mediavilla for interesting and useful discussions, and Evencio Mediavilla for confirming our results with an independent re-analysis of the SN Zwicky data. We thank the referee for suggesting the inclusion of the multipole analysis in the paper.

This work has been enabled by support from the research project grant ‘Understanding the Dynamic Universe’ funded by the Knut and Alice Wallenberg Foundation under Dnr KAW 2018.0067. EM acknowledges support from the Swedish Research Council under Dnr VR 2020-03384. ST has been supported by funding from the European Research Council (ERC) under the European Union’s Horizon 2020 research and innovation programmes (grant agreement no. 101018897 CosmicExplorer). SD acknowledges funding by UK Research and Innovation (UKRI) under the UK government’s Horizon Europe funding Guarantee EP/Z000475/1, a Kavli Fellowship and a JRF at Lucy Cavendish College. This project has received funding from the European Union’s Horizon Europe research and innovation programme under the Marie Skłodowska-Curie grant agreement No 101105725. AG acknowledges support from the Swedish Research Council (Dnr 2020-03444) and the

Swedish National Space Agency (Dnr 2023-00226). EEH is supported by a Gates Cambridge Scholarship (#OPP1144). This work has received funding from the European Research Council (ERC) under the European Union's Horizon 2020 research and innovation programme (LensEra: grant agreement No. 945536). For the purpose of open access, the authors have applied a Creative Commons Attribution (CC BY) license to any Author Accepted Manuscript version arising.

*Software used:* AstroPy (Astropy Collaboration et al. 2013, 2018, 2022), Jupyter (Kluyver et al. 2016), Matplotlib (Hunter 2007; Caswell et al. 2020), NumPy (Harris et al. 2020), Pandas (McKinney 2010; Pandas

Development Team 2023), Pickle (Van Rossum 2020), SciPy (Virtanen et al. 2020), Seaborn (Waskom et al. 2020), Emcee (Foreman-Mackey et al. 2013; Goodman & Weare 2010), ChainConsumer (Hinton 2016), Lenstronomy (Birrer & Amara 2018; Birrer et al. 2021), Prospector (Johnson et al. 2021), FSPS (Conroy et al. 2009, 2010; Conroy & Gunn 2010), Python-FSPS (Johnson et al. 2024), SEDPy (Johnson 2021), Dynesty (Speagle 2020; Koposov et al. 2024), Reproject (Robitaille et al. 2020), SAOImageDS9 (Smithsonian Astrophysical Observatory 2000; Joye & Mandel 2003).

## DATA AVAILABILITY

Code related to this article is available at <https://github.com/Nikki1510/Microlensing>

## REFERENCES

Arendse N., et al., 2024, *MNRAS*, **531**, 3509  
 Astropy Collaboration et al., 2013, *A&A*, **558**, A33  
 Astropy Collaboration et al., 2018, *AJ*, **156**, 123  
 Astropy Collaboration et al., 2022, *ApJ*, **935**, 167  
 Auger M. W., Treu T., Bolton A. S., Gavazzi R., Koopmans L. V. E., Marshall P. J., Moustakas L. A., Burles S., 2010, *ApJ*, **724**, 51  
 Bellm E. C., et al., 2019, *PASP*, **131**, 018002  
 Birrer S., Amara A., 2018, *Phys. Dark Universe*, **22**, 189  
 Birrer S., et al., 2021, *J. Open Source Software*, **6**, 3283  
 Birrer S., et al., 2024, *Space Sci. Rev.*, **220**, 48  
 Blagorodnova N., et al., 2018, *PASP*, **130**, 035003  
 Byler N., Dalcanton J. J., Conroy C., Johnson B. D., 2017, *ApJ*, **840**, 44  
 Calzetti D., Armus L., Bohlin R. C., Kinney A. L., Koornneef J., Storchi-Bergmann T., 2000, *ApJ*, **533**, 682  
 Cano Z., Selsing J., Hjorth J., de Ugarte Postigo A., Christensen L., Gall C., Kann D. A., 2018, *MNRAS*, **473**, 4257  
 Carnall A. C., Leja J., Johnson B. D., McLure R. J., Dunlop J. S., Conroy C., 2019, *ApJ*, **873**, 44  
 Carr B., Kühnel F., Sandstad M., 2016, *Phys. Rev. D*, **94**, 083504  
 Caswell T. A., et al., 2020, matplotlib/matplotlib: v3.3.2, [doi:10.5281/zenodo.4030140](https://doi.org/10.5281/zenodo.4030140)  
 Chabrier G., 2003, *PASP*, **115**, 763  
 Chang K., Refsdal S., 1979, *Nature*, **282**, 561  
 Chen W., et al., 2022, *Nature*, **611**, 256  
 Choi J., Dotter A., Conroy C., Cantiello M., Paxton B., Johnson B. D., 2016, *ApJ*, **823**, 102  
 Clesse S., García-Bellido J., 2015, *Phys. Rev. D*, **92**, 023524  
 Cohen J. S., Fassnacht C. D., O’Riordan C. M., Vegetti S., 2024, *MNRAS*, **531**, 3431  
 Conroy C., Gunn J. E., 2010, *ApJ*, **712**, 833  
 Conroy C., Gunn J. E., White M., 2009, *ApJ*, **699**, 486  
 Conroy C., White M., Gunn J. E., 2010, *ApJ*, **708**, 58  
 Decleir M., et al., 2022, *ApJ*, **930**, 15  
 Dhawan S., et al., 2020, *MNRAS*, **491**, 2639  
 Dhawan S., et al., 2024, *MNRAS*, **535**, 2939  
 Diego J. M., Bernstein G., Chen W., Goobar A., Johansson J. P., Kelly P. L., Mörtsell E., Nightingale J. W., 2022, *A&A*, **662**, A34  
 Dobler G., Keeton C. R., 2006, *ApJ*, **653**, 1391  
 Escrivà A., Kühnel F., Tada Y., 2024, in Sedda M. A., Bortolas E., Spera M., eds, Black Holes in the Era of Gravitational-Wave Astronomy. Elsevier, pp 261–377 ([arXiv:2211.05767](https://arxiv.org/abs/2211.05767))  
 Esteban-Gutiérrez A., Agües-Paszkowsky N., Mediavilla E., Jiménez-Vicente J., Muñoz J. A., Heydenreich S., 2020, *ApJ*, **904**, 176  
 Esteban-Gutiérrez A., Mediavilla E., Jiménez-Vicente J., Muñoz J. A., 2023, *ApJ*, **954**, 172  
 Ferland G. J., et al., 2013, *Rev. Mexicana Astron. Astrofís.*, **49**, 137  
 Feroz F., Hobson M. P., Bridges M., 2009, *MNRAS*, **398**, 1601  
 Fitzpatrick E. L., Massa D., Gordon K. D., Bohlin R., Clayton G. C., 2019, *ApJ*, **886**, 108  
 Foreman-Mackey D., Hogg D. W., Lang D., Goodman J., 2013, *PASP*, **125**, 306  
 Foxley-Marrable M., Collett T. E., Vernardos G., Goldstein D. A., Bacon D., 2018, *MNRAS*, **478**, 5081  
 Fremling C., Meynardie W., Yan L., Salama M., Jensen-Clem 2022, Transient Name Server AstroNote, **194**, 1  
 Frye B. L., et al., 2024, *ApJ*, **961**, 171  
 Goldstein D. A., Nugent P. E., Kasen D. N., Collett T. E., 2018, *ApJ*, **855**, 22  
 Goldstein D. A., Nugent P. E., Goobar A., 2019, *ApJS*, **243**, 6  
 Goobar A., et al., 2017, *Science*, **356**, 291  
 Goobar A., et al., 2023, *Nature Astronomy*, **7**, 1098  
 Goodman J., Weare J., 2010, *Communications Applied Math. Comput. Sci.*, **5**, 65  
 Gordon K., 2024, *J. Open Source Software*, **9**, 7023  
 Gordon K. D., Cartledge S., Clayton G. C., 2009, *ApJ*, **705**, 1320  
 Gordon K. D., et al., 2021, *ApJ*, **916**, 33  
 Gordon K. D., Clayton G. C., Decler M., Fitzpatrick E. L., Massa D., Misselt K. A., Tollerud E. J., 2023, *ApJ*, **950**, 86  
 Graham M. J., et al., 2019, *PASP*, **131**, 078001  
 Hao C. N., Mao S., Deng Z. G., Xia X. Y., Wu H., 2006, *MNRAS*, **370**, 1339  
 Harris C. R., et al., 2020, *Nature*, **585**, 357  
 Hawkins M. R. S., 2020, *A&A*, **633**, A107  
 Higson E., Handley W., Hobson M., Lasenby A., 2019, *Statistics Comput.*, **29**, 891  
 Hinton S. R., 2016, *J. Open Source Software*, **1**, 00045  
 Huber S., et al., 2019, *A&A*, **631**, A161  
 Hunter J. D., 2007, *Comput. Sci. Eng.*, **9**, 90  
 Ivezić Ž., et al., 2019, *ApJ*, **873**, 111  
 Jiménez-Vicente J., Mediavilla E., 2022, *ApJ*, **941**, 80  
 Johansson J., et al., 2021, *MNRAS*, **502**, 510  
 Johnson B. D., 2021, bd-j/sedpy: v0.2.0, [doi:10.5281/zenodo.4582723](https://doi.org/10.5281/zenodo.4582723)  
 Johnson B. D., Leja J., Conroy C., Speagle J. S., 2021, *ApJS*, **254**, 22  
 Johnson B., et al., 2024, dfm/python-fsp: v0.4.7, [doi:10.5281/zenodo.12447779](https://doi.org/10.5281/zenodo.12447779)  
 Joye W. A., Mandel E., 2003, in Payne H. E., Jedrzejewski R. I., Hook R. N., eds, Astron. Soc. Pac. Conf. Series Vol. 295, Astronomical Data Analysis Software and Systems XII. pp 489–492  
 Kashlinsky A., 2016, *ApJ*, **823**, L25  
 Katz N., Balbus S., Paczynski B., 1986, *ApJ*, **306**, 2  
 Kauffmann G., et al., 2003, *MNRAS*, **341**, 33  
 Kelly P. L., et al., 2015, *Science*, **347**, 1123  
 Kelly P., et al., 2022, Transient Name Server AstroNote, **169**, 1  
 Khlopov M. Y., 2010, *Res. Astron. Astrophys.*, **10**, 495  
 Kluyver T., et al., 2016, in Loizides F., Schmidt B., eds, Positioning and Power in Academic Publishing: Players, Agents and Agendas. IOS Press, pp 87–90, [doi:10.3233/978-1-61499-649-1-87](https://doi.org/10.3233/978-1-61499-649-1-87)  
 Koposov S., et al., 2024, joshspeagle/dynesty: v2.1.4, [doi:10.5281/zenodo.3348367](https://doi.org/10.5281/zenodo.3348367)  
 Kulkarni S. R., 2013, The Astronomer’s Telegram, **4807**, 1  
 Larison C., et al., 2024, preprint, ([arXiv:2409.17239](https://arxiv.org/abs/2409.17239))  
 Lemon C., et al., 2024, *Space Sci. Rev.*, **220**, 23

Magee M. R., Sainz de Murieta A., Collett T. E., Enzi W., 2023, *MNRAS*, **525**, 542

McKinney W., 2010, in van der Walt S., Millman J., eds, Proceedings of the 9th Python in Science Conference. pp 56–61, doi:10.25080/Majora-92bf1922-00a

Mediavilla E., Jiménez-Vicente J., 2025, in Byrnes C., Franciolini G., Harada T., Pani P., Sasaki M., eds, Primordial Black Holes. Springer Nature, Singapore, pp 577–593 (arXiv:2405.14984), doi:10.1007/978-981-97-8887-3\_23

Mediavilla E., Muñoz J. A., Lopez P., Mediavilla T., Abajas C., Gonzalez-Morcillo C., Gil-Merino R., 2006, *ApJ*, **653**, 942

Mediavilla E., et al., 2009, *ApJ*, **706**, 1451

Mediavilla E., Jiménez-Vicente J., Muñoz J. A., Vives-Arias H., Calderón-Infante J., 2017, *ApJ*, **836**, L18

More A., Suyu S. H., Oguri M., More S., Lee C.-H., 2017, *ApJ*, **835**, L25

Mortenson M. J., Schechter P. L., Wambsganss J., 2005, *ApJ*, **628**, 594

Mörtsell E., Johansson J., Dhawan S., Goobar A., Amanullah R., Goldstein D. A., 2020, *MNRAS*, **496**, 3270

Oguri M., Marshall P. J., 2010, *MNRAS*, **405**, 2579

Paczynski B., 1986, *ApJ*, **301**, 503

Pandas Development Team 2023, pandas-dev/pandas: v2.3.3, Zenodo, doi:10.5281/zenodo.3509134

Pierel J. D. R., Rodney S., 2019, *ApJ*, **876**, 107

Pierel J. D. R., Rodney S., Vernardos G., Oguri M., Kessler R., Anguita T., 2021, *ApJ*, **908**, 190

Pierel J., et al., 2022, Transient Name Server AstroNote, **196**, 1

Pierel J. D. R., et al., 2023, *ApJ*, **948**, 115

Pierel J. D. R., et al., 2024, *ApJ*, **967**, L37

Planck Collaboration et al., 2020, *A&A*, **641**, A6

Pooley D., Rappaport S., Blackburne J., Schechter P. L., Schwab J., Wambsganss J., 2009, *ApJ*, **697**, 1892

Pooley D., Rappaport S., Blackburne J. A., Schechter P. L., Wambsganss J., 2012, *ApJ*, **744**, 111

Refsdal S., 1964, *MNRAS*, **128**, 307

Rigault M., et al., 2019, *A&A*, **627**, A115

Robitaille T., Deil C., Ginsburg A., 2020, reproject: Python-based astronomical image reprojection, Astrophysics Source Code Library, record ascl:2011.023

Rodney S. A., Brammer G. B., Pierel J. D. R., Richard J., Toft S., O'Connor K. F., Akhshik M., Whitaker K. E., 2021, *Nature Astronomy*, **5**, 1118

Sagués Carracedo A., et al., 2024, preprint, (arXiv:2406.00052)

Sainz de Murieta A., Collett T. E., Magee M. R., Weisenbach L., Krawczyk C. M., Enzi W., 2023, *MNRAS*, **526**, 4296

Sainz de Murieta A., Collett T. E., Magee M. R., Pierel J. D. R., Enzi W. J. R., Lokken M., Gagliano A., Ryczkowski D., 2024, *MNRAS*, **535**, 2523

Sánchez-Blázquez P., et al., 2006, *MNRAS*, **371**, 703

Schechter P. L., Wambsganss J., 2004, in Ryder S., Pisano D., Walker M., Freeman K., eds, IAU Symp. Vol. 220, Dark Matter in Galaxies. p. 103 (arXiv:astro-ph/0309163)

Schechter P. L., Wambsganss J., Lewis G. F., 2004, *ApJ*, **613**, 77

Schechter P. L., Pooley D., Blackburne J. A., Wambsganss J., 2014, *ApJ*, **793**, 96

Schlafly E. F., Finkbeiner D. P., 2011, *ApJ*, **737**, 103

Schmidt R. W., Wambsganss J., 2010, *Gen. Relativ. Gravitation*, **42**, 2127

Shajib A. J., et al., 2019, *MNRAS*, **483**, 5649

Skilling J., 2004, in Fischer R., Preuss R., Toussaint U. V., eds, American Inst. Phys. Conf. Series Vol. 735, 24th International Workshop on Bayesian Inference and Maximum Entropy Methods in Science and Engineering. AIP, pp 395–405, doi:10.1063/1.1835238

Skilling J., 2006, *Bayesian Analysis*, **1**, 833

Smithsonian Astrophysical Observatory 2000, SAOImage DS9: A utility for displaying astronomical images in the X11 window environment, Astrophysics Source Code Library, record ascl:0003.002

Sonnenfeld A., Treu T., Gavazzi R., Suyu S. H., Marshall P. J., Auger M. W., Nipoti C., 2013, *ApJ*, **777**, 98

Speagle J. S., 2020, *MNRAS*, **493**, 3132

Suyu S. H., Goobar A., Collett T., More A., Vernardos G., 2024, *Space Sci. Rev.*, **220**, 13

Townsend A., et al., 2025, *A&A*, **694**, A146

Treu T., Marshall P. J., 2016, *A&A Rev.*, **24**, 11

Van Rossum G., 2020, The Python Library Reference, Release 3.8.2. Python Software Foundation

Vernardos G., Fluke C. J., 2013, *MNRAS*, **434**, 832

Vernardos G., Tsagkatakis G., 2019, *MNRAS*, **486**, 1944

Vernardos G., et al., 2024, *Space Sci. Rev.*, **220**, 14

Virtanen P., et al., 2020, *Nature Methods*, **17**, 261

Wambsganss J., 2006, in Meylan G., Jetzer P., North P., eds, Saas-Fee Advanced Course Vol. 33, Gravitational Lensing: Strong, Weak & Micro. Springer, Berlin, Heidelberg, pp 453–540 (arXiv:astro-ph/0604278)

Waskom M., et al., 2020, mwaskom/seaborn: v0.11.0, doi:10.5281/zenodo.4019146

Weisenbach L., 2025, *MNRAS*, **541**, 281

Weisenbach L., Schechter P. L., Pontula S., 2021, *ApJ*, **922**, 70

Weisenbach L., Collett T., de Murieta A. S., Krawczyk C., Vernardos G., Enzi W., Lundgren A., 2024, *MNRAS*, **531**, 4349

Weisenbach L., Collett T., Enzi W., Oldham L., de Murieta A. S., 2025, *MNRAS*, **539**, 393

Wojtak R., Hjorth J., Gall C., 2019, *MNRAS*, **487**, 3342

Xu D. D., Sluse D., Gao L., Wang J., Frenk C., Mao S., Schneider P., 2013, preprint, (arXiv:1307.4220)

Yahalom D. A., Schechter P. L., Wambsganss J., 2017, preprint, (arXiv:1711.07919)

Young P., 1981, *ApJ*, **244**, 756

#### A. APPENDIX: CORNER PLOTS

Fig. A.1 shows the full corner plot of all free parameters in our `prospector` fits for the stellar mass, as described in section 5.1, both for iPTF16geu and SN Zwicky.

Fig. A.2 shows the resulting parameter posteriors when SN Zwicky and iPTF16geu are combined in one single fit, where they share a common  $f_{dc}$  parameter. By combining the two, a tighter upper limit of  $f_{dc} < 0.19$  (95%) is obtained. This assumes that  $f_{dc}$  is the same at all image positions in both galaxies.

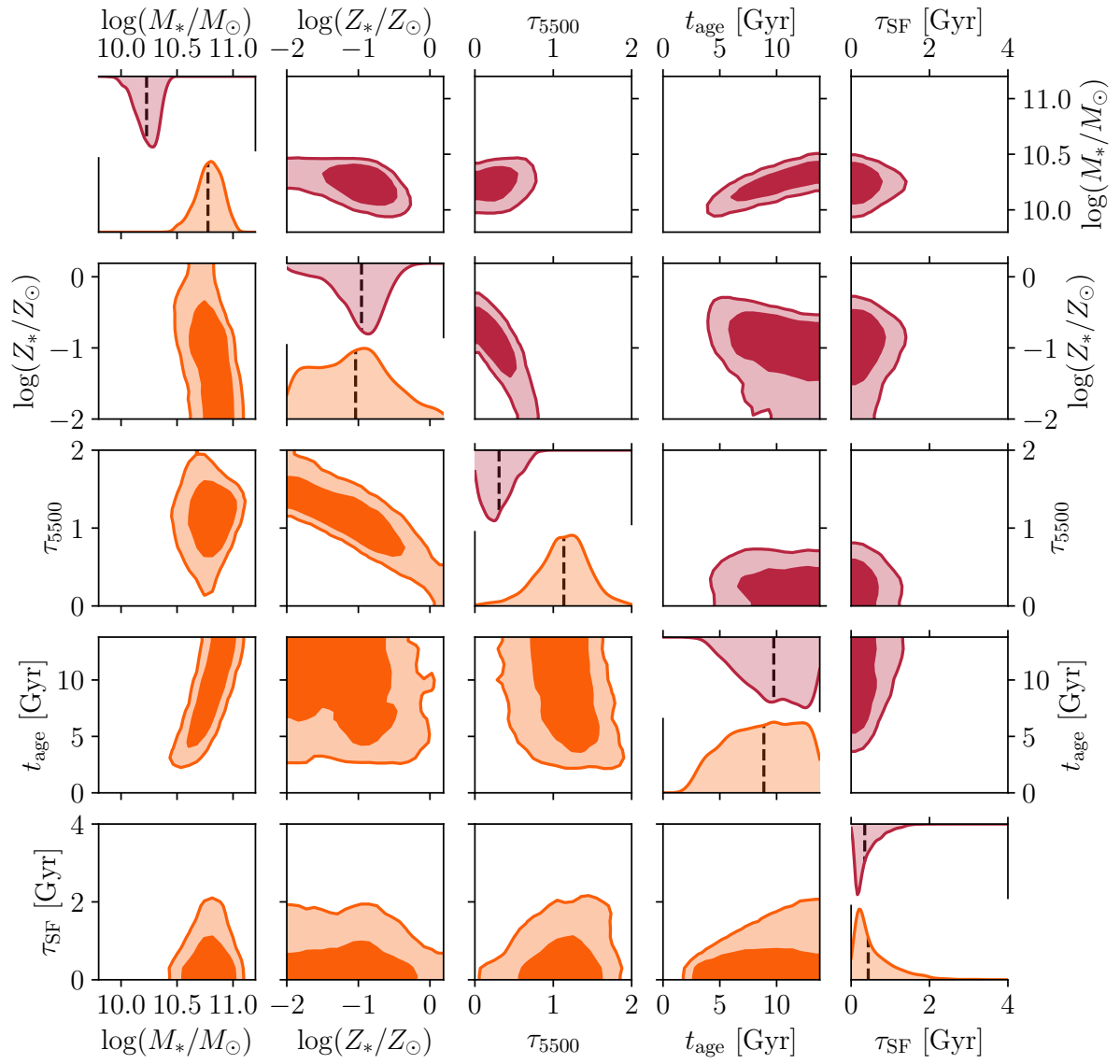


FIG. A.1.—: Cornerplot showing the free parameters in the `prospector` fits for iPTF16geu (lower and left panels) and SN Zwicky (upper and right panels).

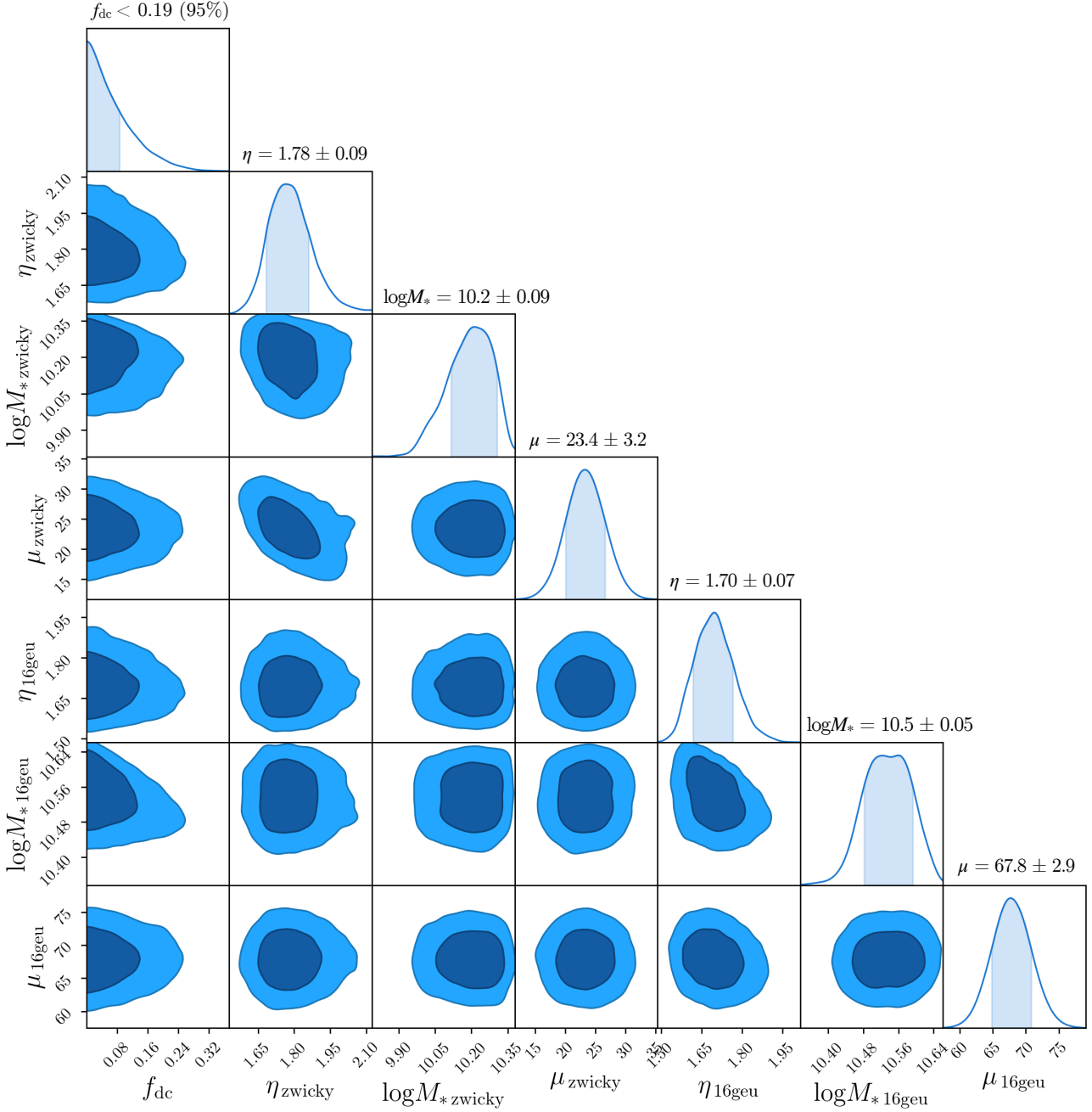


FIG. A.2.—: Joint fit for iPTF16geu and SN Zwicky. Each have individual parameters for their slopes ( $\eta$ ), stellar masses ( $\log M_*$ ), and total magnifications ( $\mu$ ), but they share a common parameter for the dark compact object fraction ( $f_{dc}$ ). This shows how multiple lensed SN can be combined to give a tighter upper limit on  $f_{dc}$ .